

1 Quantifying the Impact of SST Feedback Frequency on the 2 Madden-Julian Oscillation Simulations

3 Yung-Yao Lan¹, Huang-Hsiung Hsu¹, and Wan-Ling Tseng²

4 ¹Research Center for Environmental Changes, Academia Sinica, Taipei 11529, Taiwan

5 ²Ocean Center, National Taiwan University, Taipei 10617, Taiwan

6 *Correspondence to:* Huang-Hsiung Hsu (hhhsu@gate.sinica.edu.tw)

8 Abstract

9 This study uses the CAM5 coupled to a 1-d ocean model to investigate the effects
10 of intraseasonal SST feedback frequency on the Madden-Julian Oscillation (MJO)
11 simulation with intervals at 30 minutes, 1, 3, 6, 12, 18, 24, and 30 days. The large-scale
12 nature of the MJO in simulations remains intact with decreasing feedback frequency,
13 although becoming increasingly unrealistic in both structure and amplitude, until
14 1/30days when the intraseasonal fluctuations are overwhelmingly dominated by
15 unorganized small-scale perturbations in both atmosphere and ocean, as well as at the
16 atmosphere-ocean interface where heat and energy are rigorously exchanged. The main
17 conclusion is less frequent the SST feedback, more unrealistic the simulations. Our
18 results suggest that more spontaneous atmosphere-ocean interaction (e.g., ocean
19 response once every time step to every three days in this study) with high vertical
20 resolution in the ocean model is a key to the realistic simulation of the MJO and should
21 be properly implemented in climate models.

23 1. Introduction

24 The Madden-Julian Oscillation (MJO) is a large-scale tropical circulation that
25 propagates eastward from the tropical Indian Ocean (IO) to the western Pacific (WP)
26 with a periodicity of 30–80 days (Madden and Julian, 1972). In the Indo-Pacific region,
27 the MJO processes involve intraseasonal variability of sea surface temperature (SST)
28 (Chang et al., 2019; DeMott et al., 2014, 2015; Jiang et al., 2015, 2020; Krishnamurti

29 et al., 1998; Li et al., 2014; Li et al., 2020a; Newman et al., 2009; Pei et al., 2018; Stan,
30 2018; Tseng et al., 2015). The tropical air–sea interaction, influenced by the upper ocean,
31 plays a crucial role in determining MJO characteristics due to the high heat capacity of
32 the upper ocean within the intraseasonal range, which acts as a significant heat source
33 for atmospheric variability (Watterson, 2002; Sobel and Gildor, 2003; Maloney and
34 Sobel, 2004; Sobel et al., 2010; Liang and Du, 2022).

35 Analyzing the mechanism of the intraseasonal oscillation (ISO) reveals that heat
36 fluxes play a critical role in the development of intraseasonal SST variability (Hong et
37 al., 2017; Liang et al., 2018). As demonstrated in Fu et al. (2017), underestimation
38 (overestimation) of the air–sea coupling's impact on MJO simulations occurs when it is
39 weak (strong) in the intraseasonal SST variability. Simulation improvements in the
40 eastward propagation and regulation of MJO periodicity in the coupled models can be
41 attributed to several factors such as enhanced low-level convergence and convective
42 instability to the east of convection, as well as enhanced latent heat fluxes (Savarin and
43 Chen, 2022) and SST cooling to the west of convection (DeMott et al., 2014). SST
44 gradients have been found to induce patterns of mass convergence and divergence
45 within the marine boundary layer (MBL), initiating atmospheric convection (de Szoeki
46 and Maloney, 2020; Lambaerts et al., 2020).

47 Several recent studies have made significant progress in understanding the impact
48 of air–sea coupling on the MJO, particularly at sub-daily scales (e.g., DeMott et al.,
49 2015; Kim et al., 2018; Seo et al., 2014; Voldoire et al., 2022; Zhao and Nasuno, 2020).
50 However, there is relatively limited discussion on the effect of air–sea coupling from
51 few days to within half of the MJO period. Several studies have investigated the impact
52 of intraseasonal SST on the MJO by coupled or uncoupled models. (e.g., DeMott et al.,
53 2014; Gao et al., 2020b; Klingaman and Demott, 2020; Pariyar et al., 2023; Stan, 2018).
54 Simulations using time-varying SSTs from coupled global climate model (CGCM) to

55 force the atmospheric general circulation model (AGCM) showed a reduced
56 intraseasonal SST variability, leading to weakened air–sea heat fluxes and eastward
57 propagation (DeMott et al., 2014; Gao et al., 2020b; Klingaman and Demott, 2020;
58 Pariyar et al., 2023). Moreover, the absence of few days variability in SST promotes
59 the amplification of westward power associated with Rossby waves (Stan, 2018).

60 Incorporating two-way coupling between the ocean and atmosphere has been
61 proved valuable for simulating and predicting intraseasonal variability (e.g., DeMott et
62 al., 2014; Lan et al., 2022; Stan, 2018; Tseng et al., 2015, 2020). As demonstrated in
63 recent studies (e.g., Ge et al., 2017; Lan et al., 2022; Shinoda et al., 2021; Tseng et al.,
64 2015, 2022), incorporating high vertical resolution near the ocean surface positively
65 influences the accurate representation of intraseasonal SST variability and enhances the
66 MJO prediction capabilities. However, how frequent is the coupling needed is still not
67 fully understood, considering the fact that the ocean and atmosphere could evolve in
68 distinct time scales. And, would the coupling frequency in numerical models influence
69 the accuracy of the MJO simulation?

70 In this study, we aim to investigate the specific effects of oceanic feedback
71 frequency (FF) through air–sea coupling on the atmospheric intraseasonal variability,
72 using the National Center for Atmospheric Research (NCAR) Community Atmosphere
73 Model 5.3 (CAM5.3) coupled with the single-column ocean model named Snow–Ice–
74 Thermocline (SIT). The coupled model is referred to as CAM5–SIT. The SIT model,
75 consisting of 41 vertical layers, enables the simulation of SST and upper-ocean
76 temperature variations with high vertical resolution (Lan et al., 2022). We have
77 demonstrated in previous studies that coupling the SIT significantly improved the MJO
78 simulations in several AGCMs (Tseng et al., 2015, 2022; Lan et al., 2022). The ability
79 of the SIT with extremely high-resolutions (i.e., 12 layers within the first 10.5 m) to
80 well resolve the upper ocean warm layer and the cool skin of the ocean surface was

81 identified as the main reason for the improved simulations.

82 The structure of this paper is organized as follows. Section 2 introduces the model,
83 data, methodology, and experiments employed in this study. The performance of the
84 CAM5–SIT models in simulating the MJO is discussed in Section 3, while Section 4
85 focuses on the impact of different configurations of sub-seasonal SST feedback
86 periodicity on MJO simulations. Finally, Section 5 presents the conclusions.

87

88 **2. Data, model experiments, and methodology**

89 **2.1 Observational data**

90 Observational data sets used in this study include precipitation from the Global
91 Precipitation Climatology Project (GPCP, 1° resolution, 1997–2010; Adler et al., 2003),
92 outgoing longwave radiation (OLR, 1° resolution, 1997–2010; Liebmann, 1996), and
93 daily SST (optimum interpolated SST, OISST, 0.25° resolution, 1989–2010; Banzon et
94 al., 2014) from the National Oceanic and Atmosphere Administration, and the fifth
95 generation ECMWF reanalysis (ERA5), with a resolution of 0.25° for the period of
96 1989–2020 (Hersbach and Dee, 2016). Various variables from ERA5 were considered,
97 including winds, vertical velocity, temperature, specific humidity, sea level pressure,
98 geopotential height, latent and sensible heat, and shortwave and longwave radiation.
99 For the initial conditions of the SIT, the SST data was obtained from the Hadley Centre
100 Sea Ice and Sea Surface Temperature dataset version 1 (HadISST1), with a resolution
101 of 1° for the period of 1982–2001 (Rayner et al., 2003). The ocean subsurface data,
102 including climatological ocean temperature, salinity, and currents in 40 layers, were
103 retrieved from the National Centers for Environmental Prediction (NCEP) Global
104 Ocean Data Assimilation System (GODAS) with a resolution of 0.5° for the period of
105 1980–2012 (Behringer and Xue, 2004). These data were used for a weak nudging
106 (Tseng et al., 2015, 2022; Lan et al., 2022) in the SIT model.

107

108 **2.2 Experimental design**

109 In this study, we investigated the role of oceanic FF using coupled CAM5–SIT and
110 atmosphere-only CAM5 (A–CTL). Previous studies (Lan et al., 2022; Tseng et al., 2022)
111 have provided a detailed description of the every timestep coupling CAM5–SIT model
112 and its performance in simulating the MJO. Table 1 displays the experimental
113 configuration, incorporating monthly HadISST1 (uncoupled region) and ice
114 concentrations over a 30-year period centered around the year 2000 (F2000 compsets,
115 Rasch et al., 2019). Solar insolation, greenhouse gas and ozone concentrations, and
116 aerosol emissions representative of present-day conditions were prescribed. In the A–
117 CTL, observed monthly-mean SST around the year 2000 was prescribed to force the
118 CAM5. For the coupled simulations, we adjusted the Flux Coupler (CPL) restriction in
119 the Climate Earth System Model (CESM1; Hurrell et al., 2013) by implementing
120 asymmetric exchange frequencies between the atmosphere and the ocean. The ocean
121 continuously receives atmospheric forcing at every time step (30 minutes) and the
122 temperature changes accordingly, but the SST seen by the atmospheric model is fixed
123 at each timestep for a specified time span (e.g., 1, 3, 6, 12, 18, 24, and 30 days). That
124 is, the SST seen by the atmospheric model only changed until the end of the specified
125 time span.

126 Two sets of experiments in addition to the A–CTL were conducted, each
127 representing a different SST feedback frequency:

128 (1) High-frequency SST feedback set: This set includes the control experiment
129 (C–CTL) with SST feedback at every timestep (FF as 48/day), once a day (C–
130 1day: FF as 1/day), and every 3 days (C–3days: FF as 1/3days).

131 (2) Low-frequency SST feedback set: This set includes experiments with SST
132 feedback to the atmosphere for every 6 days (C–6days: FF as 1/6days), 12 days

133 (C–12days: FF as 1/12days), 18 days (C–18days: FF as 1/18days), 24 days (C–
134 24days: FF as 1/24days), and 30 days (C–30days: FF as 1/30days).

135 The SIT is coupled to CAM5 between 30° N to 30° S. The ocean was weakly
136 nudged (using a 30-day exponential time scale) between depths of 10.5 m and 107.8 m,
137 and strongly nudged (using a 1-day exponential time scale) below 107.8 m, based on
138 the climatological ocean temperature data from NCEP GODAS. No nudging was
139 applied in the upper-most 10.5 meters, allowing the simulation of rigorous air–sea
140 coupling near the ocean surface.

141 During the simulation, the SIT recalculated the SST within the tropical air–sea
142 coupling region. Outside this coupling region, the annual cycle of HadSST1 was
143 prescribed. No SST transition between the tropical air–sea coupling zone and the
144 extratropical SST-prescribed regions was applied. The ocean bathymetry for the SIT
145 was derived from the NOAA’s 1 arc-minute global relief model of Earth’s surface that
146 integrated land topography and ocean bathymetry (ETOPO1) data (Amante and Eakins,
147 2009). To ensure consistency and comparability, all observational, atmospheric, oceanic,
148 and reanalysis data were interpolated into a horizontal resolution of $1.9^\circ \times 2.5^\circ$ for
149 model initialization, nudging, and comparison of experimental simulations.

150

151 **2.3 Methodology**

152 The analysis focused on the boreal winter period (November–April), the season
153 with the most pronounced eastward propagation of the MJO. To identify intraseasonal
154 variability, the CLIVAR MJO Working Group diagnostics package (CLIVAR, 2009)
155 and a 20–100-day filter (Wang et al., 2014) was used. MJO phases were defined based
156 on the Real-time Multivariate MJO series 1 (RMM1) and series 2 (RMM2) proposed
157 by Wheeler and Hendon (2004), which utilized the first two principal components of
158 combined near-equatorial OLR and zonal winds at 850 and 200 hPa. The band-pass

159 filtered data were used to calculate the index and define the MJO phases.

160 Analysis of column-integrated MSE budgets was conducted to investigate the
161 association between tropical convection and large-scale circulations. The column-
162 integrated MSE budget equation (e.g., Sobel et al., 2014) is approximately given by

$$163 \left\langle \frac{\partial h}{\partial t} \right\rangle' = - \left\langle u \frac{\partial h}{\partial x} \right\rangle' - \left\langle v \frac{\partial h}{\partial y} \right\rangle' - \left\langle w \frac{\partial h}{\partial p} \right\rangle' + \langle LW \rangle' + \langle SW \rangle' + \langle SH \rangle' + \langle LH \rangle' \quad (1)$$

164 where h denotes the moist static energy

$$165 h = c_p T + gz + L_v q \quad (2)$$

166 where T is temperature (K); q is specific humidity (Kg Kg^{-1}); c_p is dry air heat capacity
167 at constant pressure ($1004 \text{ J K}^{-1} \text{ kg}^{-1}$); L_v is latent heat of condensation (taken constant
168 at $2.5 \times 10^6 \text{ J kg}^{-1}$); u and v are horizontal and meridional wind (m s^{-1}), respectively; w
169 is the vertical pressure velocity (Pa s^{-1}); LW and SW are the longwave and shortwave
170 radiation flux (W m^{-2}), respectively; and LH and SH are the latent and sensible surface
171 heat flux (W m^{-2}), respectively. The angle bracket ($\langle * \rangle$) represents mass-weighted
172 vertical integration from 1000 to 100 hPa; and the intraseasonal anomalies are
173 represented as $\langle * \rangle'$.

174

175 **3. Results**

176 **3.1 The mean state and intraseasonal variability of SST**

177 The variability of SSTs plays a crucial role in the dynamics of the MJO. Studies
178 based on observations from TOGA COARE and DYNAMO revealed that MJO events
179 exhibited a stronger ocean temperature response compared to average conditions (de
180 Szoeké et al., 2014). Wu et al. (2021) revealed the better MJO prediction skill in the
181 CGCM could be contributed by the improved representation of high-frequency SST
182 fluctuations related to the MJO, with warm (cold) SST anomalies to the east (west) of
183 MJO convection, through the convection–SST feedback processes (Li et al., 2020a; Wu

184 et al., 2021). It is therefore necessary to check on the influences of coupling and coupling
185 frequency on the SST fluctuations.

186 Table 2 presents the oceanic temperature anomalies for the DJF seasonal mean,
187 including the differences in oceanic temperature between the SST and depths of 10m
188 ($\overline{\Delta T_{0-10m}}$) and 30m ($\overline{\Delta T_{0-30m}}$), as well as 20–100 days maximum and minimum SST
189 and oceanic temperature at 10m depth (T_{10m}). The region of 110–130° E and 5–15° S
190 was selected because of the largest variation in the 20–100-day bandpass-filtered SST
191 when the MJO passes over the Indo-Pacific region. Simulated DJF seasonal mean SST
192 (300.8K to 302.0 K) are generally smaller than OISST (302.2 K) but increase with the
193 lower SST feedback frequency except in C–30days (302.7 K), while the SST standard
194 deviation remains within 0.8 K, smaller than OISST (0.96 K), except in C–24days (1.06
195 K) and C–30days (1.71 K) that implies the potential jump in SST.

196 The simulated subsurface (0–10m and 0–30m) ocean temperatures were compared
197 with those in the NCEP GODAS reanalysis and presented as ($\overline{\Delta T_{0-10m}}$ and $\overline{\Delta T_{0-30m}}$).
198 The $\overline{\Delta T_{0-10m}}$ in high-frequency experiments maintained 0.1 K temperature difference.
199 In low-frequency experiments, $\overline{\Delta T_{0-10m}}$ increased from 0.2 to 1.0 K with decreasing
200 SST feedback frequency. The temperature difference ($\overline{\Delta T_{0-30m}}$) in both high-frequency
201 and low-frequency experiments remains approximately 0.8K, except for C–24days and
202 C–30days with an increase as high as 1.4 K and 2.1 K, respectively, with larger standard
203 deviations. The comparison revealed the cooling effect of the SIT on the seasonal mean
204 SST, especially in the higher-frequency coupling experiment due to the more rigorous
205 heat exchanges between ocean and atmosphere. However, in the lower frequency
206 experiments, the SST became much warmer and so did vertical temperature differences
207 due likely to the unrealistically large heat accumulation of loss in the ocean.

208 As for the MJO simulation, the SST fluctuation is more relevant. The OISST
209 fluctuation through a MJO cycle was about ± 0.21 K. In comparison, the uncoupled A–

210 CTL, which was forced by monthly mean HadISST1, yielded a negligible SST
211 fluctuation (-0.003–0.02 K) as expected. In the high-frequency experiments, SST
212 fluctuated in magnitudes similar to that in the daily OISST. The amplitude became
213 unrealistically larger in the low-frequency coupling experiments with C–30days
214 reaching as high as 0.6 K. The increasingly larger amplitudes were likely resulted from
215 the heat accumulation in the ocean because of less frequent feedback (or heat release) to
216 the model atmosphere. Changes in coupling frequency led to different amplitudes of SST
217 fluctuation in a MJO cycle. As will be revealed latter, this effect had marked influence
218 on the MJO simulations.

219

220 **3.2 MJO simulation: high-frequency and low-frequency SST feedback experiments**

221 **3.2.1 General structure**

222 The propagation characteristics of the different experiments were analyzed using
223 the wavenumber-frequency spectrum (W-FS). The spectra of unfiltered U850 in ERA5,
224 A–CTL, and all coupling experiments with different feedback frequency are shown in
225 Fig. 1a–j. The C–CTL experiment accurately captures the eastward propagating signals
226 at zone wavenumber 1 with 30–80-day period (Fig. 1a and 1c), although with a slightly
227 larger amplitude than ERA5 (Fig. 1a). By contrast, the uncoupled A–CTL produced an
228 unrealistic spectral shift to time scales longer than 30–80 days (Fig. 1b) and simulated
229 the unrealistic westward propagation at wavenumber 2.

230 The W-FS spectra of the C–1day and C–3day experiment show two peaks for zone
231 wavenumber 1 over the 30 to 80-day period. The low-frequency experiments (i.e., from
232 C–6days to C–30days) increasingly enhanced the amplitudes and lowered the
233 frequency of intraseasonal perturbations with decreasing feedback frequency.
234 Furthermore, unrealistic westward W-FS of U850 becomes evident in (Fig. 1h–i) in the

235 C–18days, C–24days, and C–30days experiments, reflecting the stationary nature of
236 simulated MJO seen in Fig. 2i–j.

237 The Hovmöller diagrams in Fig. 2a–j depict the evolution of 10° N–10° S averaged
238 precipitation and U850 anomalies on intraseasonal timescales, represented by the
239 lagged correlation coefficients with the precipitation averaged over 10° S–5° N, 75–
240 100° E. In GPCP/ERA5, observed precipitation and U850 propagated eastward from
241 the eastern IO to the dateline, with precipitation leading U850 by approximately a
242 quarter of a cycle and a propagation speed of about 5 m s⁻¹ (Fig. 2a). The A–CTL
243 simulation was dominated by stationary features, with westward-propagating tendency
244 over the IO and weak and slow eastward propagation over the MC and WP (Fig. 2b).
245 The Hovmöller diagrams derived from high-frequency and low-frequency experiments
246 (Fig. 2c–h) display the key eastward propagation characteristics in both precipitation
247 and U850, as well as the phase relationship between them, except in C–24days and C–
248 30days that were dominated by stationary perturbations. Further decreased feedback
249 frequency from 1/C–24days to 1/C–30days also further weakened the signals of
250 precipitation and U850. More detailed discussion on this topic will be presented in the
251 subsequent chapter.

252 We conducted a wavenumber-frequency power spectral analysis (Wheeler and
253 Kiladis, 1999) to examine the phase lag and coherence between the tropical circulation
254 and convection. Figures 3a–i illustrate the symmetric part of OLR and U850 for
255 NOAA/ERA5 data and all model experiments. The MJO band exhibits a high degree
256 of coherence, indicating a strong correlation between NOAA MJO-related OLR signal
257 and wavenumbers 1–3 (Fig. 3a). The phase lag in the 30–80-day band is approximately
258 90°, consistent with previous studies (Ren et al., 2019; Wheeler and Kiladis, 1999). All
259 model experiments simulated the coherence within wavenumber 3 in the MJO band,
260 with a phase lag similar to NOAA/ERA5 data. However, the A–CTL spectrum exhibits

261 only half of the observed coherence peak at wavenumber 1, and also weaker coherence
262 at wavenumbers 2–3 for the 30–80-day period compared to NOAA/ERA5 data. The
263 experiments C–CTL, C–1day, C–3days, C–6days, C–12days, and C–18days yielded
264 wavenumber-1 coherence peak similar to that in NOAA/ERA5. Additionally, as the
265 SST feedback frequency decreases from 1/12days to 1/30days, the experiments
266 increasingly simulated unrealistic coherence in the very low frequency with a wide
267 range of zonal wavenumber from 1 to 12 (Fig. 3g–j), i.e., no zonal scale preference.

268 Figure 4 shows the phase–longitude diagrams in which the 20–100-day filtered
269 precipitation (shaded) and SST (contour) anomalies were averaged over 10° S to 10° N
270 to determine the relationship between precipitation and SST fluctuations and to provide
271 insights into the connection between air–sea coupling and convection. As expected, the
272 A–CTL did not simulate the eastward-propagating coupled SST-convection
273 perturbations as in observation (Fig. 4a), whereas C–CTL, C–1day, and C–3days
274 properly reproduced the observed features. The eastward-propagating coupled
275 perturbations were also simulated in C–6days, C–12days, and C–18days, but with
276 unrealistically increasing amplitudes near the dateline, especially in the C–18days
277 experiment. The perturbation amplification near the dateline was likely due to the lack
278 of ocean circulation in the CAM5–SIT. The amplification was also seen in C–24days
279 that failed to simulate the eastward-propagating intraseasonal perturbations. When
280 coupling frequency was reduced to 1/30days, the eastward propagation could no longer
281 be simulated and was replaced by unorganized standing oscillations in much smaller
282 zonal scales.

283 Liang et al. (2018) suggested that SST leading precipitation by 10 days implies
284 air–sea interactions at the intraseasonal timescale during MJO events, with SST playing
285 a crucial role in modulating the MJO's intensity and propagation. The A–CTL
286 simulation exhibited weak SST anomalies and stationary precipitation when using the

287 monthly average HadISST1. By contrast, the C–24days and C–30days experiment
288 showed no clear phase lag between disorganized SST and precipitation perturbations.
289 A comparison between simulation results and observation indicates that the air–sea
290 interaction plays a crucial role in facilitating eastward propagation and higher frequency
291 feedback yields more realistic simulations.

292

293 **3.2.2 Vertical structures of the MJO in the atmosphere**

294 Air–sea interaction plays a significant role in influencing atmospheric moisture and
295 convection associated with the MJO (Savarin and Chen, 2022). Whereas the ocean to
296 the east of deep convection warmed due to more downwelling shortwave radiation and
297 less heat fluxes into the atmosphere associated with weaker winds, near-surface
298 moisture convergence under the anomalous subsidence over the warmer water
299 preconditioned the eastward movement of the deep convection (DeMott et al., 2015;
300 Zhang, 2005). The MJO was noted to detour southward when crossing the MC region,
301 exhibiting enhanced convective activity preferentially in the southern MC area and
302 weaker convection in the central MC area (Hsu and Lee, 2005; Wu and Hsu, 2009; Kim
303 et al., 2017). Hovmöller diagrams in Fig. 5a–j illustrate the relationship between the
304 vertical structure of air temperature (contoured, in K) and specific humidity (shading,
305 in g kg^{-1}) anomalies from the surface to 200 hPa averaged over 5–20° S and 120–150°
306 E. In ERA5, the lower-level positive temperature anomaly in phase 3 (i.e.,
307 preconditioning phase) leads the development of deep temperature and moisture
308 anomalies (i.e., deep convection) after phase 4 over the MC, when moisture anomalies
309 reached the maxima at 700–500 hPa. This two-phase upward development was not
310 properly simulated in A–CTL, which shows sudden switch between positive and
311 negative anomalies in the entire troposphere, instead of progressively upward
312 development with time. The upward development was generally simulated in coupled

313 simulations from C-CTL to C-6days (Fig. 5c-e), although the negative temperature
314 anomalies below 500 hPa were over-simulated after phase 5. It became less well
315 simulated beyond C-12days and was gradually replaced by sudden phase switch as in
316 the A-CTL, especially in C-30days (Fig. 5f-j). The preconditioning phase completely
317 disappears in C-18 days and beyond. As identified in previous studies, the two-phase
318 upward development is a manifestation of air-sea coupling. The missing of this
319 coupling evidently resulted in the poor simulation in the A-CTL and extremely low
320 feedback frequency experiments.

321

322 **3.2.3 Vertical structures of the MJO in the ocean**

323 The 1-D turbulence kinetic energy (TKE) ocean model incorporates a high vertical
324 resolution that captures the vertical gradient of temperature in the upper ocean. Figure
325 6 (left column) illustrates the vertical structures of oceanic temperature between 0- and
326 60-meters during phase 2-3 when the deep convection occurred over the eastern IO
327 (60-90° E) and easterly anomalies prevailed over the MC and western Pacific. In the
328 high-frequency experiments (Fig. 6a, 6c, 6e), the upper oceanic temperatures exhibit
329 warming patterns within 30 meters depth at 100-140° E (i.e., east of the deep
330 convection and under the easterly anomalies), apparently due to more downwelling
331 short wave radiation and less heat flux release to the atmosphere. By contrast, the
332 cooling near the dateline was associated with westerly anomalies. With decreasing
333 feedback frequency, the cooling to the east of 150°E seen in high frequency experiments
334 was replaced by oceanic warming that amplified with further feedback frequency
335 decrease. The warming region that became more widespread and larger amplitude with
336 less frequent feedback eventually grew to cover the entire IO and WP, an area much
337 larger than the scale of the atmospheric MJO. The mismatch between the atmospheric
338 and oceanic anomalies suggested the weakening atmospheric-ocean coupling that

339 resulted in poor simulation of the MJO in the low frequency feedback simulations. The
340 emergence of small-scale unorganized structures with decreasing feedback frequency
341 is also evident in phase 4–5 (right column of Fig. 6), e.g., negative ocean temperature
342 anomalies in the Indian Ocean under the prevailing westerly anomalies.

343

344 **4. Discussion**

345 **4.1 Dynamic lead–lag relationship in intraseasonal variability**

346 The lead–lag relationship refers to a situation where one variable (leading) is
347 cross-correlated with the values of another variable (lagging) in subsequent phases,
348 particularly in the case of SST fluctuations and MJO-related atmospheric variations
349 between phase 1 and 8 within the domain of 110–130° E and 5–15° S (Fig. 7). The
350 analyzed variables include 20–100-day filtered latent heat flux (LHF, indicated by green
351 shading), OLR (indicated by a yellow bar chart), net surface solar radiation (FSNS,
352 indicated by an orange bar chart), U850 (indicated by a purple bar chart), 30-meter
353 depth oceanic temperature (30-m T multiplied by 100, indicated by a black line), and
354 SST (multiplied by 10, indicated by an orange line). Positive value in LHF and FSNS
355 represents an upward flux from ocean to atmosphere.

356 Decrease in LHF, which indicates a reduction in heat loss from the ocean, and
357 negative FSNS, indicating that solar radiation is heating the ocean, coincide with
358 easterly anomaly that contributes to positive SST anomaly in ERA5 (Fig. 7a). Reversed
359 fluxes are associated with westerly anomalies. This lead–lag relationship depicts the in-
360 situ atmospheric forcing on the oceanic variability during a MJO. As the MJO
361 convection progresses through the region (110–130° E and 5–15° S), several changes
362 in atmospheric and oceanic variables occur. These changes include a shift in OLR from
363 positive to negative values, a decrease in SST, a transition to westerly winds, and an
364 increase in positive FSNS and LHF (Fig. 7a). The temporal variations in SST anomaly

365 from C-CTL to C-12days were predominantly influenced by FSNS, with LHF playing
366 a secondary role, similar to the findings of Gao et al. (2020a). With the exception of
367 experiments of A-CTL, C-24days, and C-30days, both the high-frequency and low-
368 frequency SST feedback experiments simulated similar lead-lag relationships as in
369 ERA5 (Fig. 7c-h). In the C-24days and C-30days experiments, LHF was the largest
370 flux term (note the different vertical scale for the two experiments) whereas the wind,
371 OLR, and FSNS anomalies were much weaker than in other experiments. In the A-CTL
372 experiment, which was forced by monthly HasISST1 data, the SST anomalies were
373 small as expected, whereas fluxes although weak are still evident in response to
374 atmospheric perturbations (Fig. 7b). Conversely, in both C-24days and C-30days
375 experiments, a misalignment in the lead-lag relationship was observed, accompanied
376 by weak anomalies in OLR and FSNS. (Fig. 7i and 7j). This disparity between LHF and
377 wind was likely due to the unrealistically widespread and large oceanic warming as
378 shown in Fig. 6m and 6o.

379 In the simulations, the maximum positive anomaly in 30-m T was delayed by one
380 phase compared to SST, indicating the transfer of heat from the ocean surface into the
381 upper ocean progressively. Similarly, the occurrence of the most negative 30-m T
382 anomaly was also delayed by one phase compared to SST, revealing the buffering role
383 of the upper ocean when the atmospheric component of the MJO extracted (or deposited)
384 heat (energy) from (in) the ocean (Fig. 7c-i). This delayed effect was also evident in
385 the field campaign. de Szoeke et al. (2015) observed that the warmest 10-m ocean
386 temperature occurred a few days later than the peak temperature at 0.1 m. Additionally,
387 the 0.1-m ocean temperature was typically as warm as or warmer than the 10-m
388 temperature as seen in Fig. 6. In the extreme low frequency feedback experiments, the
389 amplitude of 30-m temperature became unrealistically large due likely to the continuous
390 accumulation or loss of the ocean heat.

391

392 **4.2 Unorganized perturbations in extreme frequency feedback scenarios**

393 DeMott et al. (2014) noted that in uncoupled experiments, the NCAR CAM
394 superparameterized version 3 (SPCAM3) exhibited strong eastward propagation when
395 5-day running mean SST was prescribed, but relatively weaker propagation for monthly
396 mean SST. This raises the question of how much SST feedback periodicity is necessary
397 to maintain robust eastward propagation in coupled experiments. This tendency was
398 also seen in our study, that is, slower propagation (or weaker tendency) with decreased
399 feedback frequency until the C-24days experiment (Figs. 1-7). By 1/30days, the
400 perturbations became stationary.

401 Generally, C-18days exhibited the unrealistic overestimation of intraseasonal
402 variability while maintaining eastward propagation of the MJO. Here, we are not
403 suggesting that C-18days represents the optimal SST feedback experiment. Figure 8
404 highlights the considerable differences in the simulation of MJO perturbations at phase
405 2-3 between C-18days and C-30days experiments. In C-18days, negative OLR
406 anomalies were widespread from the western IO to the MC, while in reality it should
407 be observed mainly in the IO and be accompanied by positive anomalies in the eastern
408 MC, i.e., a west-east dipolar structure (Fig. 8a). In C-30days, the OLR anomaly,
409 although was still the dominant feature in the Indian Ocean-western Pacific region,
410 became much weaker and characterized by smaller scale perturbations. These OLR
411 anomalies were generally associated with upper-level convergence (not shown)
412 embedded in much weaker wind anomalies (U200) compared to those in C-18days.
413 The circulation and OLR in C-24days exhibited the characteristics similar to those in
414 C-18days but with the OLR anomalies breaking up into smaller scales.

415 Furthermore, in the C-18days and C-24days experiments, negative anomalies
416 indicative of a downward direction in LHF and net surface heat flux (Fig. 8d, 8e, 8g,

417 and 8h), were predominantly observed in the convection-inactive region to the east of
418 150°E where low-level easterly wind and positive SST anomalies prevailed (Fig. 8j and
419 8k). The OLR, winds, heat fluxes, and SST to the west of 150°E exhibited similar
420 correspondences between variables but in opposite phase. With feedback frequency
421 reduced to 1/30days (Fig. 8f, 8i, and 8l), the heat fluxes and SST anomalies broke into
422 unorganized smaller scale features, consistent with the ocean temperature jump shown
423 in Fig. 6h. Although the wind fields in the both upper and lower levels were still
424 characterized by large-scale structure, the corresponding divergence were dominated
425 by much smaller scale perturbations (not shown), similar to heat fluxes and SST. The
426 increasingly dominant smaller scale perturbations can also be inferred from Fig. 2h–j
427 and 4h–j. In addition, the large power spectra in the low frequency band spread across
428 a wide range of wavenumbers, reflecting the smaller scale nature of the simulated
429 perturbations in C–30days (Fig. 3j). This disparity between the scale of rotational and
430 divergent winds suggests that the poor coupling between the convection and large-scale
431 circulation.

432 With decreased feedback frequency of SST from C–CTL to C–30days, the ocean
433 continued to receive atmospheric forcing, but the feedback response was delayed,
434 leading to the accumulation or loss of energy (temperature) in the upper ocean, as seen
435 in the SST distribution in the WP (Fig. 6 and 8). Subsequently, the C–30days
436 experiment exhibited comprehensive disorder over the Indo-Pacific region, with the
437 SST anomalies showing an unrealistically erratic spatial distribution characterized by
438 sudden jumps (Fig. 8l) associated with plus-minus latent heat flux and 10m wind
439 anomalies (Fig. 8f), net surface heat flux, and solar radiation (Fig. 8i). As a result, the
440 organized large-scale circulation seen in the MJO was not manifested. To this extreme,
441 the air–sea interaction observed in the MJO no longer worked properly in the model.

442

443 4.3 Moist static energy (MSE) budget analysis

444 We diagnosed the relative contribution of each term in Eq. (1) to the MSE tendency
445 with a focus on the second (pre-conditioning) and fifth (convection crossing the MC)
446 phases. Figure 9 illustrates the physical processes associated with each term (averaged
447 over 10°S – 0° , 120 – 150°E) contributing to the column-integrated MSE tendency
448 ($\langle \text{dmdt} \rangle$) in Eq. (1) during phase 2 in ERA5 and model simulations. In ERA5, when
449 the MJO convection was in the eastern Indian Ocean, the column-integrated vertical
450 and horizontal advection ($-\langle \text{wdm} \rangle$ and $-\langle \text{vdm} \rangle$) over the MC area were the dominant
451 terms in the MSE budget and largely compensated by longwave radiation and latent
452 heat flux, as reported in Wang and Li (2020) and Tseng et al. (2022). All experiments
453 simulated the positive and negative contributions similar to those derived from ERA5
454 although with different amplitudes. Notably, the C–24days and C–30days simulated
455 relatively weak vertical advection and too strong negative latent heat flux and too weak
456 longwave radiation flux. As a result, the C–24days and C–30days simulated relatively
457 weak tendency compared to other experiments. The results are consistent with the poor
458 simulation of the MJO in the extreme low frequency feedback experiments discussed
459 above.

460 We compared the spatial distribution of column-integrated MSE tendency $\langle \text{dmdt} \rangle$
461 (shading), precipitation (contours), and 850-hPa wind (vectors) during phase 5, i.e., the
462 period when the strongest convection crossing the MC (Fig. 10). In ERA5, the main
463 convection (indicated by positive precipitation anomaly) is accompanied by low-level
464 convergence in the 850-hPa wind across the MC extending into the WP (Fig. 10a). A
465 positive $\langle \text{dmdt} \rangle$ is observed to the east of the MJO convection to the south of the
466 equator (Fig. 10a). Conversely, a negative tendency is observed to the west of the MJO
467 convection accompanied by negative precipitation anomalies further to the west. The
468 phase relationship between the MSE tendency and precipitation reflects the eastward-

469 propagating nature of the MJO. With the exception of A-CTL, C-24days, and C-
470 30days, the model simulations displayed a similar structure in the 20-100-day filtered
471 <dmdt>, precipitation, and 850-hPa wind vectors (Fig. 10c-h). although the exact
472 locations may be shifted compared to those derived from ERA5. The C-CTL simulated
473 relatively weak signals compared to ERA5, whereas the signals became increasingly
474 stronger with decreasing feedback frequency. The signals became unrealistically strong
475 beyond 1/18days feedback frequency and the lead-lag relationship between the MSE
476 tendency and precipitation became less clear. For example, positive precipitation
477 anomaly became in phase with the tendency in the western Pacific south of the equator
478 in C-24days and C-30days experiments, and the tendency was much weaker in C-
479 30days. The results were consistent with the weaker eastward propagation tendency in
480 the low-frequency feedback experiments, especially in C-24days and C-30days when
481 the feedback frequency became unrealistically low.

482 The corresponding MSE budget during phase 5 is shown in Fig. 10. The MC
483 has been identified as a barrier to the eastward propagation of the MJO (Hsu and Lee,
484 2005; Wu and Hsu, 2009; Tseng et al., 2017; Li et al., 2020b) and approximately 30-
485 50% of the MJO experienced stalling over the MC (Zhang and Han, 2020). To
486 determine whether the MJO has sufficient energy to traverse the MC, we focused the
487 analysis on phase 5. Figure 11 illustrates the projection of each MSE component and
488 decomposition of the horizontal MSE advection at phase 5 over the MC region (20° S-
489 20° N, 90-210° E) following the approach of Tseng et al. (2022) and Jiang et al. (2018),
490 where F_s is total surface fluxes including SH and LH, and Q_r is vertically integrated net
491 SW and LW radiation. Unlike in phase 2 when vertical advection is the dominant term,
492 the MSE tendency was dominated by the horizontal MSE advection -<vdm> in ERA5
493 and all experiments, except the A-CTL. This contribution increased with decreasing
494 SST feedback frequency. The weaker positive vertical advection -<wdmdp> did not

495 vary systematically with decreasing feedback frequency and even turned negative in
496 C–24days and C–30days. F_s and Q_r acted to damp the tendency by cancelling out the
497 effect of the advection term. F_s tended to be more negative with decreasing feedback
498 frequency and became much larger in C–30days. By contrast, Q_r was unrealistically
499 weak in C–18days, C–24days, and C–30days. The uncoupled simulation yielded much
500 weaker amplitude in all terms as expected.

501 The $\langle vdm \rangle$ that contributed most to the eastward propagation of the MJO in
502 phase 5 was further decomposed into zonal ($\langle udmx \rangle$) and meridional ($\langle vmdy \rangle$)
503 components to examine their relative effects (Fig. 11). Both components contributed
504 positively, but the $\langle vmdy \rangle$ exhibited a larger amplitude, consistent with Tseng et al.
505 (2015, 2022). The $\langle vmdy \rangle$ of high-frequency SST feedback experiments yielded
506 results closely similar to ERA5. Comparatively, the $\langle vmdy \rangle$ term in low-frequency
507 SST feedback experiments (C–18days, C–24days, and C–30days) became
508 unrealistically large with decreasing feedback frequency and the potential jump in SST.

509 Spatial distributions of $\langle wmdp \rangle$, $\langle vdm \rangle$, and 200-hPa wind at phase 5 are
510 shown in Fig. 12. In ERA5, the wind divergence at 200 hPa at phase 5 (Fig. 12a),
511 overlaid the 850-hPa convergence (Fig. 10a), reflecting a deep convection structure.
512 The model simulations exhibited a similar structure to ERA5 except in A–CTL, C–
513 24days, and C–30days experiments, and again the amplitude increased with decreasing
514 feedback frequency. In ERA5, negative $\langle wmdp \rangle$ and $\langle vdm \rangle$ anomalies (Fig. 12a)
515 were observed to the west of the MJO convection (Fig. 10a). The spatial distribution of
516 the negative $\langle vdm \rangle$ anomaly (dashed-red contours) extends from the IO to the MC
517 and positive anomaly (predominantly meridional advection from the south, not shown)
518 in the western-central Pacific south of the equator tends to facilitate the eastward
519 propagation of deep convection in the western Pacific, consistent with Tseng et al.
520 (2015, 2022). The $\langle wmdp \rangle$ with negative and positive anomaly to the west and east

521 of the deep convection also contributes to the eastward propagation of the MJO, but
522 with weaker contribution than $\langle vdm \rangle$. Again, these characteristics were not simulated
523 in A-CTL, whereas the amplitudes of both terms became increasingly larger with
524 decreasing feedback frequency until becoming unrealistically large beyond 1/18days.
525 In C-30days experiment both terms exhibited unorganized spatial structure as shown
526 in preceding discussion. In summary, the high-frequency feedback experiments
527 simulated an approximately 80% projection of $\langle vdm \rangle$ in ERA5, whereas the low-
528 frequency SST feedback experiments overestimated $\langle vdm \rangle$ anomalies (Fig. 12f-h).

529

530 **5. Conclusions**

531 This study built upon the work of Lan et al. (2022) and Tseng et al. (2022) by
532 coupling a high-resolution 1-D TKE ocean model (the SIT model) with the CAM5, i.e.,
533 a CAM5-SIT configuration, to investigate the effects of intraseasonal SST feedback on
534 the MJO. We introduced asymmetric exchange frequencies between the atmosphere and
535 the ocean, ensuring bidirectional interaction at each timestep within the experimental
536 periodicity by fixing the SST value in the coupler. This allowed us to create SST
537 feedback with various intervals at 30 minutes, 1, 3, 6, 12, 18, 24, and 30 days.

538 The aim is to assess the effect of SST feedback frequency, namely, how often
539 should the atmosphere-driven SST change feedback to the atmosphere and whether
540 there is a limit. With the exception of the C-24days and C-30days experiment, both the
541 high-frequency and low-frequency experiments demonstrated realistic simulations of
542 various aspects of the MJO when compared to ERA5, GPCP, and OISST data, although
543 the simulation results becoming increasingly amplified and unrealistic with decreasing
544 feedback frequency. These aspects included intraseasonal periodicity (Fig. 1), eastward
545 propagation (Fig. 2 and 4), coherence in the intraseasonal band (Fig. 3), tilting vertical
546 structure (Fig. 5), intraseasonal SST (Table 2) and oceanic temperature variances (Fig.

547 6), the lead–lag relationship of intraseasonal variability (Fig. 7), contribution of each
548 term to the column-integrated MSE tendency at the preconditioning phase (phase 2)
549 and mature phased (phase 5) (Fig. 9 and Fig. 11). The MSE tendency term was
550 dominated by the horizontal and vertical MSE advection in phase 5 and phase 2,
551 respectively, in ERA5 and most experiments. Furthermore, we deliberately extended
552 the SST feedback interval to an unrealistically long 30 days to investigate the limits of
553 delayed ocean response. The main conclusion is less frequent the update, more
554 unrealistic the simulation result.

555 The lead–lag relationship provides a visual representation of the variations in 20–
556 100-day filtered LHF, FSNS, OLR, U850 and SST with positive SST anomaly leading
557 the onset of the MJO convection (Fig. 7). This relationship highlights the
558 interconnected nature of surface heat fluxes, solar radiation, and atmospheric
559 circulation patterns, underscoring their mutual influence and interplay through air–sea
560 interaction. Our results indicate that the high-frequency (low-frequency) SST
561 experiments tended to underestimate (overestimate) the MJO simulation in CAM5–SIT
562 model. Whether this finding can be applied to other models warrants further
563 investigations.

564 The result of C–3days experiment is consistent with Stan (2018), suggesting the
565 absence of 1–5-day variability in SST would promote the amplification of westward
566 power associated with tropical Rossby waves. By comparing with the control
567 experiment in which SST feedback occurs at every time step (30 minutes), the C–1day
568 experiment (SST feedback once daily) confirmed the findings of Hagos et al. (2016)
569 and Lan et al. (2022) that the removal of the diurnal cycle would enhance the MJO. The
570 increasing feedback periodicity of SST in low-frequency experiments led to the
571 accumulation of atmospheric influences through short-wave and long-wave radiations
572 and surface heat fluxes, resulting in an unrealistically large ocean temperature

573 anomalies and variances within few tens of meters below ocean surface (Table 2). The
574 large-scale nature of the MJO remains intact with decreasing feedback frequency,
575 although becoming increasingly unrealistic in both structure and amplitude, until
576 1/30days when the intraseasonal fluctuations were overwhelmingly dominated by
577 unorganized small-scale perturbations in both atmosphere and ocean, as well as at the
578 atmosphere-ocean interface where heat and energy were rigorously exchanged.

579 The reason causing the sudden change between C-24days and C-30days is not
580 entirely clear. Two possibilities are discussed here. The first possible reason leading to
581 this disorder is that when the ocean feedback is delayed for as long as 30 days (more
582 than half of the MJO period) both positive and negative fluxes would contribute to the
583 heat accumulation or loss in the ocean because of the MJO phase transition and result
584 in unorganized small scale structures in ocean temperatures, which could in turn affect
585 the heat flux and convection. The second possible reason would be that the SST
586 variation in a MJO event become more abrupt and may disrupt the large-scale nature of
587 the MJO into disorganized spatial distribution in atmosphere, ocean, and the interface
588 where rigorous heat exchange occurs. This disrupting effect of abrupt SST variation,
589 which is not explored in this study, warrants further studies with purposely designed
590 experiment to untangle.

591 Finally, results of intraseasonal SST feedback experiments on MJO are
592 summarized schematically in Fig. 13, following DeMott et al. (2014). These
593 experiments included the uncoupled experiment (A-CTL), high-frequency SST
594 experiments (C-CTL, C-1day, and C-3days), low-frequency SST experiments (C-
595 6days, C-12days, and C-18days), and extreme low-frequency experiment (C-24days
596 and C-30days). In the absence of intraseasonal SST variability, the eastward
597 propagation of the MJO was disrupted, leading to weakened or fragmented MJO
598 activity as shown in Fig. 13a. On the other hand, the high-frequency SST experiments

599 closely mimicked air–sea interaction and well captured the characteristics of the MJO.
600 The time-varying SSTs in the coupled simulation provided a certain degree of
601 organization and sufficient surface fluxes, which facilitated the development of the
602 MJO circulation as illustrated in Fig. 13b. The horizontal moist static energy tendency
603 derived from increased low-level convergence, especially due to the meridional
604 advection of MSE, intensified the MJO convection and triggered the eastward
605 propagation over the MC region. The PBL convergence ahead of the MJO convection
606 is due to Kelvin-wave dynamics (Jiang, 2017), in conjunction with the background
607 zonal flow structure (Tulich and Kiladis, 2021). Horizontal MSE or moisture advection
608 in the lower troposphere, particularly the seasonal mean low-level MSE influenced by
609 the MJO's anomalous winds, has had a significant impact on the MJO propagation.
610 (Gonzalez and Jiang, 2017; Jiang, 2017). This simulation result is consistent with the
611 understanding that the MJO is primarily attributed to the interaction between organized
612 convection and large-scale circulations that triggers the eastward propagation. As
613 feedback frequency become lower, the major characteristics of the MJO could still be
614 simulated as depicted in Fig. 13c, but with overestimated amplitudes and deteriorating
615 simulations in spatial structures. In the extreme low frequency experiments with
616 frequency decreasing to 1/24days and 1/30days, unorganized structures started to
617 emerge and broke up into smaller scale perturbations as shown in Fig. 13d, when large-
618 scale air–sea interaction embedded in the MJO did not operate properly in the model.
619 Eventually in the C–30days experiment, unrealistically and spatially scattered
620 anomalies in precipitation, jumping SST, surface heat fluxes, and vertical and
621 horizontal MSE advection became dominant features. All these findings led to the
622 major conclusion of this study: more spontaneous atmosphere-ocean interaction (e.g.,
623 ocean response once every time step to every three days in this study) with high vertical

624 resolution in the ocean model is a key to the realistic simulation of the MJO and should
625 be properly implemented in climate models.

626

627 *Code and data availability.* The model code of CAM5–SIT is available at
628 <https://doi.org/10.5281/zenodo.5510795>. Input data of CAM5–SIT using the
629 climatological Hadley Centre Sea Ice and Sea Surface Temperature dataset and
630 GODAS data forcing, including 30-year numerical experiments, are available at
631 <https://doi.org/10.5281/zenodo.5510795>.

632

633 *Author contributions.* YYL is the CAM5–SIT model developer and writes the majority
634 part of the paper. HHH contributes to the physical explanation and the reorganization
635 and revision of the manuscript. WLT assists in the MSE analysis.

636

637 *Competing interests.* The authors declare that they have no conflict of interest.

638

639 *Acknowledgements.* Our deepest gratitude goes to the editors and anonymous reviewers
640 for their careful work and thoughtful suggestions that have helped improve this paper
641 substantially. We sincerely thank the National Center for Atmospheric Research
642 (NCAR) and their Atmosphere Model Working Group (AMWG) for release
643 CESM1.2.2. We are also grateful to the National Center for High- performance
644 Computing, Taiwan for providing the facilities for the computational procedures for
645 running MJO simulations. Thanks, ChatGPT for correcting the English grammar.

646

647 *Financial support.* This research received funding from the Taiwan National Science
648 and Technology Council under Grants NSTC 112-2111-M-001-008 and MOST 111-
649 2123-M-001-007, as well as support from the Academia Sinica Grand Challenge

650 Program in Taiwan under Grant AS-GCP-112-M03.

651

652 **Reference**

653 Adler, R. F., Huffman, G. J., Chang, A., Ferraro, R., Xie, P.
654 P., Janowiak, J., Rudolf, B., Schneider, U., Curtis, S., Bolvin,
655 D., Gruber, A., Susskind, J., Arkin, P., and Nelkini, E.: The Version
656 2.1 Global Precipitation Climatology Project (GPCP) Monthly
657 Precipitation Analysis (1979 -Present), *J. Hydrometeor.*, 4(6), 1147-
658 1167, [https://doi.org/10.1175/1525-
659 7541\(2003\)004<1147:TVGPCP>2.0.CO;2](https://doi.org/10.1175/1525-7541(2003)004<1147:TVGPCP>2.0.CO;2), 2003.

660 Amante, C., and Eakins, B. W.: ETOPO1 1 arc-minute globe relief model:
661 Procedures, data sources and analysis, NOAA Tech. Memo. NESDIS
662 NGDC-24, NOAA, Silver Spring, MD, 19 pp.,
663 <https://doi.org/10.7289/V5C8276M>, 2009.

664 Banzon, V. F., Reynolds, R. W., Stokes, D., and Xue, Y.: A 1/4-spatial-
665 resolution daily sea surface temperature climatology based on a
666 blended satellite and in situ analysis, *J. Climate*, 27, 8221–8228,
667 <https://doi.org/10.1175/JCLI-D-14-00293.1>, 2014.

668 Behringer, D. W., and Xue, Y.: Evaluation of the global ocean data
669 assimilation system at NCEP: The Pacific Ocean. Eighth Symposium
670 on Integrated Observing and Assimilation Systems for Atmosphere,
671 Oceans, and Land Surface, AMS 84th Annual Meeting, Washington
672 State Convention and Trade Center, Seattle, Washington, 11-15.
673 Derber, J.C., and A. Rosati, 1989: A global oceanic data assimilation
674 system, *J. Phys. Oceanogr.*, 19, 1333–1347,
675 <https://ams.confex.com/ams/pdfpapers/70720.pdf>, 2004.

676 Chang, M.-Y., Li, T., Lin, P.-L., and Chang, T.-H.: Forecasts of MJO
677 Events during DYNAMO with a Coupled Atmosphere-Ocean Model:
678 Sensitivity to Cumulus Parameterization Scheme, *J. Meteorol. Res.*,
679 33, 1016–1030, <https://doi.org/10.1007/s13351-019-9062-5>, 2019.

680 CLIVAR MADDEN–JULIAN OSCILLATION WORKING GROUP: MJO
681 simulation diagnostics, *J. Climate*, 22, 3006–3030,
682 <https://doi.org/10.1175/2008JCLI2731.1>, 2009.

683 DeMott, C. A., Klingaman, N. P., and Woolnough, S. J.: Atmosphere-
684 ocean coupled processes in the Madden-Julian oscillation, *Rev. of*
685 *Geophysics*, 53, 1099– 1154, [https://doi.org/10.1002/2014RG00047
686 8](https://doi.org/10.1002/2014RG000478), 2015.

687 DeMott, C. A., Stan, C., Randall, D. A., and Branson, M.
688 D.: Intraseasonal variability in coupled GCMs: The roles of ocean
689 feedbacks and model physics, *J.*
690 *Climate*, 27(13), 4970– 4995. [https://doi.org/10.1175/JCLI-D-13-
691 00760.1.](https://doi.org/10.1175/JCLI-D-13-00760.1), 2014.

692 de Szoeki, S. P., Edson, J. B., Marion, J. R., Fairall, C. W., and Bariteau,

693 L.: The MJO and air–sea interaction in TOGA COARE and
694 DYNAMO, *J. Climate*, 28(2), 597– 622. <https://doi.org/10.1175/JCLI-D-14-00477.1>, 2014.

697 de Szoeker, S. P., Edson, J. B., Marion, J. R., Fairall, C. W., and Bariteau,
698 L.: The MJO and air–sea interaction in TOGA COARE and
699 DYNAMO, *J. Climate*, 28, 597–622, <https://doi.org/10.1175/JCLI-D-14-00477.1>, 2015.

701 de Szoeker, S. P., and Maloney, E.: Atmospheric mixed layer
702 convergence from observed MJO sea surface temperature
703 anomalies, *J. Climate*, 33(2), 547– 558. <https://doi.org/10.1175/JCLI-D-19-0351.1>, 2020.

706 Fu, J. X., Wang, W., Shinoda, T., Ren, H. L., and Jia, X.: Toward
707 understanding the diverse impacts of air–sea interactions on MJO
708 simulations, *J. Geophys. Res.- Oceans*, 122(11), 8855– 8875. <https://doi.org/10.1002/2017JC013187>, 2017.

711 Gao, Y., Hsu, P.-C., Chen, L., Wang, L., and Li, T.: Effects of high-
712 frequency surface wind on the intraseasonal SST associated with the
713 Madden-Julian oscillation, *Clim. Dynam.*, 54, 4485–4498,
714 <https://doi.org/10.1007/s00382-020-05239-w>, 2020a.

715 Gao, Y., Klingaman, N. P., DeMott, C. A., and Hsu, P.-C.: Boreal
716 summer intraseasonal oscillation in a superparameterized general
717 circulation model: effects of air–sea coupling and ocean mean state,
718 *Geosci. Model Dev.*, 13, 5191–5209, <https://doi.org/10.5194/gmd-13-5191-2020>, 2020b.

720 Ge, X., Wang, W., Kumar, A., and Zhang, Y.: Importance of the vertical
721 resolution in simulating SST diurnal and intraseasonal variability in
722 an oceanic general circulation model, *J. Climate*, 30, 3963–
723 3978, <https://doi.org/10.1175/JCLI-D-16-0689.1>, 2017.

724 Gonzalez, A. O., and Jiang, X.: Winter mean lower tropospheric moisture
725 over the maritime continent as a climate model diagnostic metric for
726 the propagation of the Madden-Julian Oscillation, *Geophys. Res. Lett.*, 44(5), 2588–2596. <https://doi.org/10.1002/2016GL072430>,
727 2017.

729 Hagos, S. M., Zhang, C., Feng, Z., Burleyson, C. D., Mott, C. De, Kerns,
730 B., Benedict, J. J., and Martini, M. N.: The impact of the diurnal
731 cycle on the propagation of Madden-Julian Oscillation convection
732 across the Maritime Continent, *J. Adv. Model. Earth Syst.*, 8, 1552–
733 1564, <https://doi.org/10.1002/2016MS000725>, 2016.

734 Hersbach, H., and Dee, D.: ERA5 reanalysis is in production, ECMWF
735 Newsletter, Vol. 147, p.
736 7, <https://www.ecmwf.int/en/newsletter/147/news/era5-reanalysis->

- 737 production, 2016.
- 738 Hong, X., Reynolds, C. A., Doyle, J. D., May, P., and O'Neill, L.:
739 Assessment of upper-ocean variability and the Madden-Julian
740 Oscillation in extended-range air–ocean coupled mesoscale
741 simulations, *Dyn. Atmos. Oceans*, 78, 89–105.
742 <https://doi.org/10.1016/j.dynatmoce.2017.03.002>, 2017.
- 743 Hsu, H.-H., and Lee, M.-Y.: Topographic effects on the eastward
744 propagation and initiation of the Madden-Julian Oscillation, *J.*
745 *Climate*, 18, 795–809, <https://doi.org/10.1175/JCLI-3292.1>, 2005.
- 746 Hurrell, J. W., Holland, M. M., Gent, P. R., Ghan, S., Kay, J. E., Kushner,
747 P. J., Lamarque, J.-F., Large, W. G., Lawrence, D., Lindsay, K.,
748 Lipscomb, W. H., Long, M. C., Mahowald, N., Marsh, D. R., Neale,
749 R. B., Rasch, P., Vavrus, S., Vertenstein, M., Bader, D., Collins, W.
750 D., Hack, J. J., Kiehl, J., and Marshall, S.: The Community Earth
751 System Model: A framework for collaborative research, *Bull. Amer.*
752 *Meteor. Soc.*, 94, 1339–1360, [https://doi.org/10.1175/BAMS-D-12-](https://doi.org/10.1175/BAMS-D-12-00121.1)
753 [00121.1](https://doi.org/10.1175/BAMS-D-12-00121.1), 2013.
- 754 Jiang, X., Waliser, D. E., Xavier, P. K., Petch, J., Klingaman, N. P.,
755 Woolnough, S. J., Guan, B., Bellon, G., Crueger, T., DeMott, C.,
756 Hannay, C., Lin, H., Hu, W., Kim, D., Lappen, C.-L., Lu, M.-M.,
757 Ma, H.-Y., Miyakawa, T., Ridout, J. A., Schu-bert, S. D., Scinocca,
758 J., Seo, K.-H., Shindo, E., Song, X., Stan, C., Tseng, W.-L., Wang,
759 W., Wu, T., Wu, X., Wyser, K., Zhang, G. J., and Zhu, H.: Vertical
760 structure and physical processes of the Madden-Julian oscillation:
761 Exploring key model physics in climate simulations, *J. Geophys.*
762 *Res.-Atmos.*, 120, 4718–4748,
763 <https://doi.org/10.1002/2014JD022375>, 2015.
- 764 Jiang, X.: Key processes for the eastward propagation of the Madden-
765 Julian Oscillation based on multimodel simulations, *J. Geophys. Res.*
766 *Atmos.*, 122, 755–770, <https://doi.org/10.1002/2016JD025955>, 2017.
- 767 Jiang, X., Adames, Á. F., Zhao, M., Waliser, D., and Maloney, E.: A
768 unified moisture mode framework for seasonality of the Madden–
769 Julian oscillation, *J. Climate*, 31, 4215–4224,
770 <https://doi.org/10.1175/JCLI-D-17-0671.1>, 2018.
- 771 Jiang, X., Adames, Á. F., Kim, D., Maloney, E. D., Lin, H., and Kim, H.,
772 Zhang, C., DeMott, C. A., and Klingaman, N. P.: Fifty years of
773 research on the Madden-Julian Oscillation: Recent progress,
774 challenges, and perspectives, *J. Geophys. Res.-Atmos.*, 125,
775 e2019JD030911, <https://doi.org/10.1029/2019JD030911>, 2020.
- 776 Kim, D., Kim, H., and Lee, M.-I.: Why does the MJO detour the Maritime
777 continent during Austral summer? *Geophys. Res. Lett.*, 44(5), 2579–
778 2587, <https://doi.org/10.1002/2017gl072643>, 2017.
- 779 Kim, H., Vitart, F., and Waliser, D. E.: Prediction of the Madden–Julian
780 oscillation: A review, *J. Climate*, 31(23), 9425–9443,

- 781 <https://doi.org/10.1175/JCLI-D-18-0210.1>, 2018.
- 782 Klingaman, N. P., and Demott, C. A.: Mean state biases and interannual
783 variability affect perceived sensitivities of the Madden-Julian
784 oscillation to air–sea coupling, *J. Adv. Model. Earth Syst.*, 12, 1– 22,
785 <https://doi.org/10.1029/2019MS001799>, 2020.
- 786 Krishnamurti, T. N., Oosterhof, D. K. and Mehta, A. V.: Air–sea
787 interaction on the time scale of 30 to 50 days, *J. Atmos. Sci.*, 45,
788 1304–1322, [https://doi.org/10.1175/1520-
789 0469\(1988\)045,1304:AIOTTS.2.0.CO;2](https://doi.org/10.1175/1520-0469(1988)045,1304:AIOTTS.2.0.CO;2), 1988.
- 790 Lambaerts, J., Lapeyre, G., Plougonven, R., and Klein, P.: Atmospheric
791 response to sea surface temperature mesoscale structures, *J.*
792 *Geophys. Res.-Atmos.*, 118(17), 9611–9621.
793 <https://doi.org/10.1002/jgrd.50769>, 2020.
- 794 Lan, Y.-Y., Hsu, H.-H., Tseng, W.-L., and Jiang, L.-C.: Embedding a
795 one-column ocean model in the Community Atmosphere Model 5.3
796 to improve Madden–Julian Oscillation simulation in boreal winter,
797 *Geosci. Model Dev.*, 15, 5689–5712, [https://doi.org/10.5194/gmd-
798 15-5689-2022](https://doi.org/10.5194/gmd-15-5689-2022), 2022.
- 799 Li, Y., Han, W., Shinoda, T., Wang, C., Ravichandran, M., and Wang,
800 J.-W.: Revisiting the wintertime intraseasonal SST variability in the
801 tropical south Indian Ocean: Impact of the ocean interannual
802 variation, *J. Phys. Oceanogr.*, 44, 1886–1907,
803 <https://doi.org/10.1175/JPO-D-13-0238.1>, 2014.
- 804 Li, T., Ling, J., and Hsu, P.-C.: Madden–Julian Oscillation: Its discovery,
805 dynamics, and impact on East Asia, *J. Meteor. Res.*, 34, 20–42,
806 <https://doi.org/10.1007/s13351-020-9153-3>, 2020a.
- 807 Li, K., Yu, W., Yang, Y., Feng, L., Liu, S., and Li, L.: Spring barrier to
808 the MJO eastward propagation, *Geophys. Res. Lett.*, 47, e2020GL087788, <https://doi.org/10.1029/2020GL087788>,
809 2020b.
810
- 811 Liang, Y.; Du, Y.; Zhang, L.; Zheng, X.; Qiu, S. The 30–50-Day
812 Intraseasonal Oscillation of SST and Precipitation in the South
813 Tropical Indian Ocean, *Atmos.*, 9, 69.
814 <https://doi.org/10.3390/atmos9020069>, 2018.
- 815 Liang, Y., and Du, Y.: Oceanic impacts on 50–80-day intraseasonal
816 oscillation in the eastern tropical Indian Ocean, *Clim. Dynam.*, 59,
817 1283–1296, <https://doi.org/10.1007/s00382-021-06041-y>, 2022.
- 818 Liebmann, B.: Description of a complete (interpolated) outgoing
819 longwave radiation dataset, *B. Am. Meteorol. Soc.*, 77, 1275–1277,
820 1996.
- 821 Madden, R. A., and Julian, P. R.: Description of global-scale circulation
822 cells in the tropics with a 40-50 day period, *J. Atmos. Sci.*, 29, 1109–
823 1123, <https://doi.org/10.1175/1520->

- 824 0469(1972)029<1109:DOGSCC>2.0.CO;2, 1972.
- 825 Maloney, E., and Sobel, A. H.: Surface fluxes and ocean coupling in the
826 tropical intraseasonal oscillation. *J. Climate*, 17, 4368–4386,
827 <https://doi.org/10.1175/JCLI-3212.1>, 2004.
- 828 Newman, M., Sardeshmukh, P. D., and Penland, C.: How important is
829 air–sea coupling in ENSO and MJO evolution? *J.*
830 *Climate*, 22, 2958– 2977, <https://doi.org/10.1175/2008JCLI2659.1>,
831 2009.
- 832 Pariyar, S. K., Keenlyside, N., Tseng, W.-L., Hsu, H.-H., and Tsuang,
833 B.-J. The role of air–sea coupling on November–April intraseasonal
834 rainfall variability over the South Pacific, *Clim. Dynam.*, 60, 1121–
835 1136, <https://doi.org/10.1007/s00382-022-06354-6>, 2023.
- 836 Pei, S., Shinoda, T., Soloviev, A., and Lien, R.-C.: Upper ocean response
837 to the atmospheric cold pools associated with the Madden-Julian
838 Oscillation, *Geophys. Res. Lett.*, 45, 5020–5029,
839 <https://doi.org/10.1029/2018GL077825>, 2018.
- 840 Rasch, P. J., Xie, S., Ma, P.-L., Lin, W., Wang, H., Tang, Q., Bur-
841 rows, S. M., Caldwell, P., Zhang, K., Easter, R. C., Cameron-
842 Smith, P., Singh, B., Wan, H., Golaz, J.-C., Harrop, B. E., Roesler, E.,
843 Bacmeister, J., Larson, V. E., Evans, K. J., Qian, Y., Taylor, M.,
844 Leung, L. R., Zhang, Y., Brent, L., Branstet-
845 ter, M., Hannay, C., Mahajan, S., Mametjanov, A., Neale, R., Richter, J. H., Yoon, J.-H.,
846 Zender, C. S., Bader, D., Flan-
847 ner, M., Foucar, J. G., Jacob, R.,
848 Keen, N., Klein, S. A., Liu, X., Salinger, A. G., Shrivastava, M., and
849 Yang, Y.: An overview of the atmospheric component of the Energy
850 Exascale Earth System Model, *J. Adv. Model Earth Syst.*, 11, 2377–
2411, <https://doi.org/10.1029/2019ms001629>, 2019.
- 851 Rayner, N. A., Parker, D. E., Horton, E. B., Folland, C. K., Alexander,
852 L. V., Rowell, D. P., Kent, E. C., and Kaplan, A.: Global analyses
853 of sea surface temperature, sea ice, and night marine air temperature
854 since the late nineteenth century, *J. Geophys. Res.*, 108(D14), 4407,
855 <https://doi.org/10.1029/2002JD002670>, 2003.
- 856 Ren, P. F., Gao, L., Ren, H.-L., Rong, X., and Li, J.: Representation of
857 the Madden–Julian Oscillation in CAMSCSM, *J. Meteor. Res.*, 33,
858 627–650, <https://doi.org/10.1007/s13351-019-8118-x>, 2019.
- 859 Savarin, A., and Chen, S. S.: Pathways to better prediction of the MJO:
860 2. Impacts of atmosphere-ocean coupling on the upper ocean and
861 MJO propagation, *J. Adv. Model. Earth Syst.*, 14, e2021MS002929,
862 <https://doi.org/10.1029/2021MS002929>, 2022.
- 863 Shinoda, T., Pei, S., Wang, W., Fu, J. X., Lien, R.-C., Seo, H.,
864 and Soloviev, A.: Climate process team: Improvement of ocean
865 component of NOAA climate forecast system relevant to Madden-
866 Julian Oscillation simulations, *J. Adv. Model. Earth Syst.*, 13(12),
867 e2021MS002658. <https://doi.org/10.1029/2021MS002658>, 2021.

- 868 Seo, H., Subramanian, A. C., Miller, A. J., and Cavanaugh, N.
869 R.: Coupled impacts of the diurnal cycle of sea surface temperature
870 on the Madden–Julian oscillation, *J.*
871 *Climate*, 27(22), 8422– 8443. [https://doi.org/10.1175/JCLI-D-14-](https://doi.org/10.1175/JCLI-D-14-00141.1)
872 00141.1, 2014.
- 873 Sobel, A. H., and Gildor, H.: A simple time-dependent model of SST hot
874 spots. *J. Climate*, 16, 3978–3992, [https://doi.org/10.1175/1520-](https://doi.org/10.1175/1520-0442(2003)016<3978:ASTMOS>2.0.CO;2)
875 0442(2003)016<3978:ASTMOS>2.0.CO;2, 2003.
- 876 Sobel, A. H., Maloney, E. D., Bellon, G., and Frierson, D. M.: Surface
877 Fluxes and Tropical Intraseasonal Variability: a Reassessment, *J.*
878 *Adv. Model. Earth Syst.*, 2, 2,
879 <https://doi.org/10.3894/JAMES.2010.2.2>, 2010.
- 880 Sobel, A., Wang, S., and Kim, D.: Moist static energy budget of the MJO
881 during DYNAMO, *J. Atmos. Sci.*, 71(11), 4276– 4291,
882 <https://doi.org/10.1175/JAS-D-14-0052.1>, 2014.
- 883 Stan, C.: The role of SST variability in the simulation of the MJO, *Clim.*
884 *Dynam.*, 51, 2943–2964, [https://doi.org/10.1007/s00382-017-4058-](https://doi.org/10.1007/s00382-017-4058-2)
885 2, 2018.
- 886 Tseng, W.-L., Tsuang, B.-J., Keenlyside, N. S., Hsu, H.-H. and Tu, C.-
887 Y.: Resolving the upper-ocean warm layer improves the simulation
888 of the Madden-Julian oscillation, *Clim. Dynam.*, 44, 1487–1503,
889 <https://doi.org/10.1007/s00382-014-2315-1>, 2015.
- 890 Tseng, W.-L., Hsu, H.-H., Keenlyside, N., Chang, C.-W. J., Tsuang, B.-
891 J., Tu, C.-Y., and Jiang, L.-C.: Effects of Orography and Land–Sea
892 Contrast on the Madden–Julian Oscillation in the Maritime
893 Continent: A Numerical Study Using ECHAM-SIT, *J. Climate*, 30,
894 9725–9741, <https://doi.org/10.1175/JCLI-D-17-0051.1>, 2017.
- 895 Tseng, W.-L., Hsu, H.-H., Lan, Y.-Y., Lee, W.-L., Tu, C.-Y., Kuo, P.-
896 H., Tsuang, B.-J., and Liang, H.-C.: Improving Madden–Julian
897 oscillation simulation in atmospheric general circulation models by
898 coupling with a one-dimensional snow–ice–thermocline ocean
899 model, *Geosci. Model Dev.*, 15, 5529–5546,
900 <https://doi.org/10.5194/gmd-15-5529-2022>, 2022.
- 901 Tulich, S. N., and Kiladis, G. N.: On the Regionality of moist kelvin
902 waves and the MJO: The critical role of the background zonal flow,
903 *J. Adv. Model. Earth Syst.*, 13(9), e2021MS002528.
904 <https://doi.org/10.1029/2021MS002528>, 2021.
- 905 Voldoire, A., Roehrig, R., Giordani, H., Waldman, R., Zhang, Y., Xie,
906 S., and Bouin, M.-N.: Assessment of the sea surface temperature
907 diurnal cycle in CNRM-CM6-1 based on its 1D coupled
908 configuration, *Geosci. Model Dev.*, 15, 3347–3370,
909 <https://doi.org/10.5194/gmd-15-3347-2022>, 2022.
- 910 Wang, W., Hung, M.-P., Weaver, S. J., Kumar, A., and Fu, X.: MJO
911 prediction in the NCEP Climate Forecast System version 2, *Clim.*

- 912 Dynam., 42, 2509–2520, [https://doi.org/10.1007/s00382-013-1806-](https://doi.org/10.1007/s00382-013-1806-9)
913 9, 2014.
- 914 Wang, L. and Li, T.: Effect of vertical moist static energy advection on
915 MJO eastward propagation: Sensitivity to analysis domain, *Clim.*
916 *Dynam.*, 54, 2029–2039, [https://doi.org/10.1007/s00382-019-](https://doi.org/10.1007/s00382-019-05101-8)
917 05101-8, 2020.
- 918 Watterson, I. G.: The sensitivity of subannual and intraseasonal tropical
919 variability to model ocean mixed layer depth, *J. Geophys. Res.*, 107,
920 4020, <https://doi.org/10.1029/2001JD000671>, 2002.
- 921 Wheeler, M. C., and Hendon, H. H.: An all-season real-time multivariate
922 MJO index: development of an index for monitoring and prediction,
923 *Mon. Weather Rev.*, 132, 1917–1932, [https://doi.org/10.1175/1520-](https://doi.org/10.1175/1520-0493(2004)132<1917:AARMMI>2.0.CO;2)
924 0493(2004)132<1917:AARMMI>2.0.CO;2, 2004.
- 925 Wheeler, M., and Kiladis, G. N.: Convectively coupled equatorial waves:
926 Analysis of clouds and temperature in the wavenumber-frequency
927 domain, *J. Atmos. Sci.*, 56, 374– 399, [https://doi.org/10.1175/1520-](https://doi.org/10.1175/1520-0469(1999)056<0374:CCEWAO>2.0.CO;2)
928 0469(1999)056<0374:CCEWAO>2.0.CO;2, 1999.
- 929 Wu, C.-H., and Hsu, H.-H.: Topographic Influence on the MJO in the
930 Maritime Continent, *J. Climate*, 22, 5433–5448,
931 <https://doi.org/10.1175/2009JCLI2825.1>, 2009.
- 932 Wu, J., Li, Y., Luo, J.-J. and Jiang, X.: Assessing the role of air–sea
933 coupling in predicting Madden–Julian oscillation with an
934 Atmosphere–Ocean coupled model, *J. Clim.* 34 9647–63,
935 <https://doi.org/10.1175/JCLI-D-20-0989.1>, 2021.
- 936 Zhang, C.: Madden-Julian oscillation, *Rev. Geophys.*, 43, RG2003,
937 <https://doi.org/10.1029/2004RG000158>, 2005.
- 938 Zhang, L., and Han, W.: Barrier for the eastward propagation of
939 Madden–Julian Oscillation over the maritime continent: A possible
940 new mechanism, *Geophys. Res. Lett.*, 47(21),
941 e2020GL090211. <https://doi.org/10.1029/2020gl090211>, 2020.
- 942 Zhao, N., and Nasuno, T.: How Does the Air–Sea Coupling Frequency
943 Affect Convection During the MJO Passage?, *J. Adv. Model. Earth*
944 *Sy.*, 12, e2020MS002058, <https://doi.org/10.1029/2020MS002058>,
945 2020.

946 Table 1. Two sets of experiments with different SST feedback
 947 frequencies: high-frequency (C-CTL, C-1day and C-3days) and low-
 948 frequency (C-6days, C-12days, C-18days, C-24days and C-30days).

949

subseasonal sets	high-frequency SST (< 6 days)			low-frequency SST (6-30 days)				
experiments	C-CTL	C-1day	C-3days	C-6days	C-12days	C-18days	C-24days	C-30days
atmosphere to ocean frequency	48/1day							
ocean to atmosphere Frequency	48/1day	1/1day	1/3days	1/6days	1/12days	1/18days	1/24days	1/30days

950

951 Table 2. Key intraseasonal (20–100-day bandpass filtered) ocean temperatures in all
 952 experiments: SST, differences between SST and temperatures at 10m depth ($\overline{\Delta T}_{0-10m}$)
 953 and 30m depth ($\overline{\Delta T}_{0-30m}$), t max/mini SST and 10m-depth temperature (T_{10m}) in the
 954 area of (110–130° E, 5–15° S) during a MJO cycle for the observation (OISST), AGCM
 955 (A–CTL), high-frequency experiments (C–CTL, C–1day, and C–3days), and low-
 956 frequency experiments (C–6days, C–12days, C–18days, C–24days, and C–30days)
 957

(110–130° E, 5–15° S)		obs.	AGC M	high-frequency			low-frequency				
experiments		OI SST ¹	A– CTL ²	C– CTL	C– 1day	C– 3days	C– 6days	C– 12days	C– 18days	C– 24days	C– 30days
DJF seasonal mean	SST	302.2 ±0.96	302.2 ±0.77	300.8 ±0.76	301.2 ±0.76	301.2 ±0.75	301.2 ±0.75	301.4 ±0.75	301.6 ±0.80	302.0 ±1.06	302.7 ±1.71
	$\overline{\Delta T}_{0-10m}$	-	-	0.1 ± 0.22	0.1 ± 0.22	0.1 ± 0.21	0.1 ± 0.23	0.2 ± 0.25	0.3 ± 0.32	0.5 ± 0.50	1.0 ± 0.95
	$\overline{\Delta T}_{0-30m}$	-	-	0.8 ± 0.79	0.7 ± 0.70	0.6 ± 0.69	0.8 ± 0.70	0.8 ± 0.70	1.0 ± 0.73	1.4 ± 0.96	2.1 ± 1.54
phase's mean in boreal winter	max (phase) SST	0.21 (ph2)	0.02 (ph2)	0.24 (ph3)	0.26 (ph3)	0.22 (ph3)	0.32 (ph3)	0.36 (ph3)	0.43 (ph3)	0.50 (ph3)	0.62 (ph2)
	max T_{10m} (phase)	-	-	0.15 (ph4)	0.17 (ph4)	0.14 (ph3)	0.19 (ph3)	0.21 (ph3)	0.26 (ph3)	0.30 (ph3)	0.35 (ph2)
	mini (phase) SST	-0.21 (ph7)	-0.003 (ph8)	-0.17 (ph7)	-0.22 (ph7)	-0.19 (ph7)	-0.25 (ph7)	-0.28 (ph7)	-0.38 (ph7)	-0.52 (ph6)	-0.60 (ph6)
	mini T_{10m} (phase)	-	-	-0.11 (ph8)	-0.12 (ph7)	-0.11 (ph8)	-0.15 (ph7)	-0.17 (ph7)	-0.24 (ph7)	-0.33 (ph6)	-0.33 (ph6)

958 Note: ¹daily average data, ² monthly average data.

959 **Figure List**

960 **Figure 1.** Wavenumber–frequency spectra for 850-hPa zonal wind averaged over 10°
961 S–10° N in boreal winter after removing the climatological mean seasonal cycle.
962 Vertical dashed lines represent periods at 80 and 30 days. (a)–(j) are from ERA5
963 reanalysis, A–CTL, C–CTL, C–1day, C–3days, C–6days, C–12days, C–18days, C–
964 24days, and C–30days, respectively.

965

966 **Figure 2.** Hovmöller diagrams of correlation between precipitation averaged over 10°
967 S–5° N, 75–100° E and precipitation (color) and 850-hPa zonal wind (contour)
968 averaged over 10° N–10° S. (a)–(j) are arranged in the same order as in Fig. 1 for
969 GPCP/ERA5 and all experiments. All data are 20–100-day bandpass filtered.

970

971 **Figure 3.** Zonal wavenumber–frequency power spectra of anomalous OLR (colors) and
972 phase lag with U850 (vectors) for the symmetric component of tropical waves, with the
973 vertically upward vector representing a phase lag of 0° and phase lag increasing
974 clockwise. Three dispersion straight lines with increasing slopes representing the
975 equatorial Kelvin waves (derived from the shallow water equations) corresponding to
976 three equivalent depths, 12, 25, and 50 m, respectively. (a)–(j) are arranged in the same
977 order as in Fig. 1 for NOAA/ERA5 and all experiments.

978

979 **Figure 4.** Phase-longitude Hovmöller diagrams of 20–100-day filtered precipitation
980 (mm day^{-1} , shaded) and SST anomaly (K, contour) averaged over 10° N–10° S from
981 phase 1 to 8. Contour interval is 0.03; solid, dashed, and thick-black lines represent
982 positive, negative, and zero values, respectively. (a)–(j) are arranged in the same order
983 as in Fig. 1 for NOAA/ERA5 and all experiments.

984

985 **Figure 5.** Phase-vertical Hovmöller diagrams of 20–100-day specific humidity
986 (g kg^{-1} , shading) and air temperature (contoured, K) averaged over 5–20° S, 120–150°
987 E; solid, dashed, and thick-black curves are positive, negative, and zero values,
988 respectively. (a)–(j) are arranged in the same order as in Fig. 1 for NOAA/ERA5 and
989 all experiments.

990

991 **Figure 6.** The 20–100-day filtered oceanic temperature (K, shaded and contour,
992 interval 0.03) at phase 2–3 (Left column) and phase 4–5 (Right column) averaged
993 over 0–15° S between 0 and 60 m depth. (a)–(b) are from C–CTL, (c)–(d) are from
994 C–1day, (e)–(f) are from C–3days, (g)–(h) are from C–6days, (i)–(j) are from C–
995 12days, (k)–(l) are from C–18days, (m)–(n) are from C–24days, and (o)–(p) are from
996 C–30days.

997

998 **Figure 7.** The lead–lag relationship between MJO-related atmosphere and SST
999 variation from phase 1 to 8 averaged within 110–130° E and 5–15° S. The variables
1000 analyzed include 20–100-day filtered LHF, green shading), OLR (yellow bar chart),
1001 FSNS, (orange bar chart), U850 (purple bar chart), 30-m T (multiplied by 100, black
1002 line), and SST (multiplied by 10, orange line). Variables denoted with L (R) are scaled
1003 by the left (right) y-axis. (a)–(j) are from ERA5/OISST reanalysis, A–CTL, C–CTL, C–
1004 1day, C–3days, C–6days, C–12days, C–18days, C–24days, and C–30days, respectively.
1005

1006 **Figure 8.** Averaged 20–100-day filtered fields at phase 2–3. (Upper row) OLR (W m^{-2} ,
1007 shaded) and 200 hPa zonal and meridional wind anomaly (m s^{-1} , vector with reference
1008 vector shown at the top right corner, latent heat flux (W m^{-2} , shaded, positive
1009 representing upward), and 10-m wind anomaly (m s^{-1} , contour interval 0.5). (Second
1010 row) net surface heat flux (W m^{-2} , shaded) and net solar radiation (W m^{-2} , contour
1011 interval 6). (Third row) SST (K, shaded) and 850 hPa zonal and meridional wind
1012 anomaly (m s^{-1} , vector with reference vector shown at the top right corner. The number
1013 of days used to generate the composite is shown at the bottom right corner. (a), (d), (g)
1014 and (j) are from C–18days; (b), (e), (h) and (k) are from C–24days, and (c), (f), (i) and
1015 (l) are from C–30days, respectively. Solid, dashed, and thick-black lines represent
1016 positive, negative, and zero values, respectively.
1017

1018 **Figure 9.** Averaged 20–100-day filtered column-integrated MSE budget terms
1019 ($\text{J kg}^{-1} \text{s}^{-1}$) in 10° S–0° N/S, 120–150° E for ERA5 and all model simulations. Colors
1020 represent different datasets: green for REA5, light blue for A–CTL, red, orange and
1021 navy blue for high-frequency experiments (C–CTL, C–1day, and C–3days,
1022 respectively), purple, black, dark brown, dark green, and dark gray for low-frequency
1023 experiments (C–6days, C–12days, C–18days, C–24days, and C–30days, respectively).
1024 The bars from left to right represent MSE tendency ($\langle \text{dmdt} \rangle$), vertical MSE advection
1025 ($-\langle \text{wdmdp} \rangle$), horizontal MSE advection ($-\langle \text{vdm} \rangle$), surface latent heat flux (LH),
1026 surface sensible heat flux (SH), shortwave radiation flux ($\langle \text{SW} \rangle$), longwave radiation
1027 flux ($\langle \text{LW} \rangle$), and residual terms.
1028

1029 **Figure 10.** Filtered the column-integrated MSE tendency ($\text{J kg}^{-1} \text{s}^{-1}$, shading),
1030 precipitation (mm d^{-1} , contours interval 1.5) and 850-hPa wind (green vector, reference
1031 vector 2 m s^{-1}) in phase 5: (a) ERA5, (b) A–CTL, (c) C–CTL, (d) C–1day, (e) C–3days,
1032 (f) C–6days, (g) C–12days, (h) C–18days, (i) C–24days, and (j) C–30days. Solid-red,
1033 dashed-blue, and thick-black curves represent positive, negative, and zero values,
1034 respectively.

1035

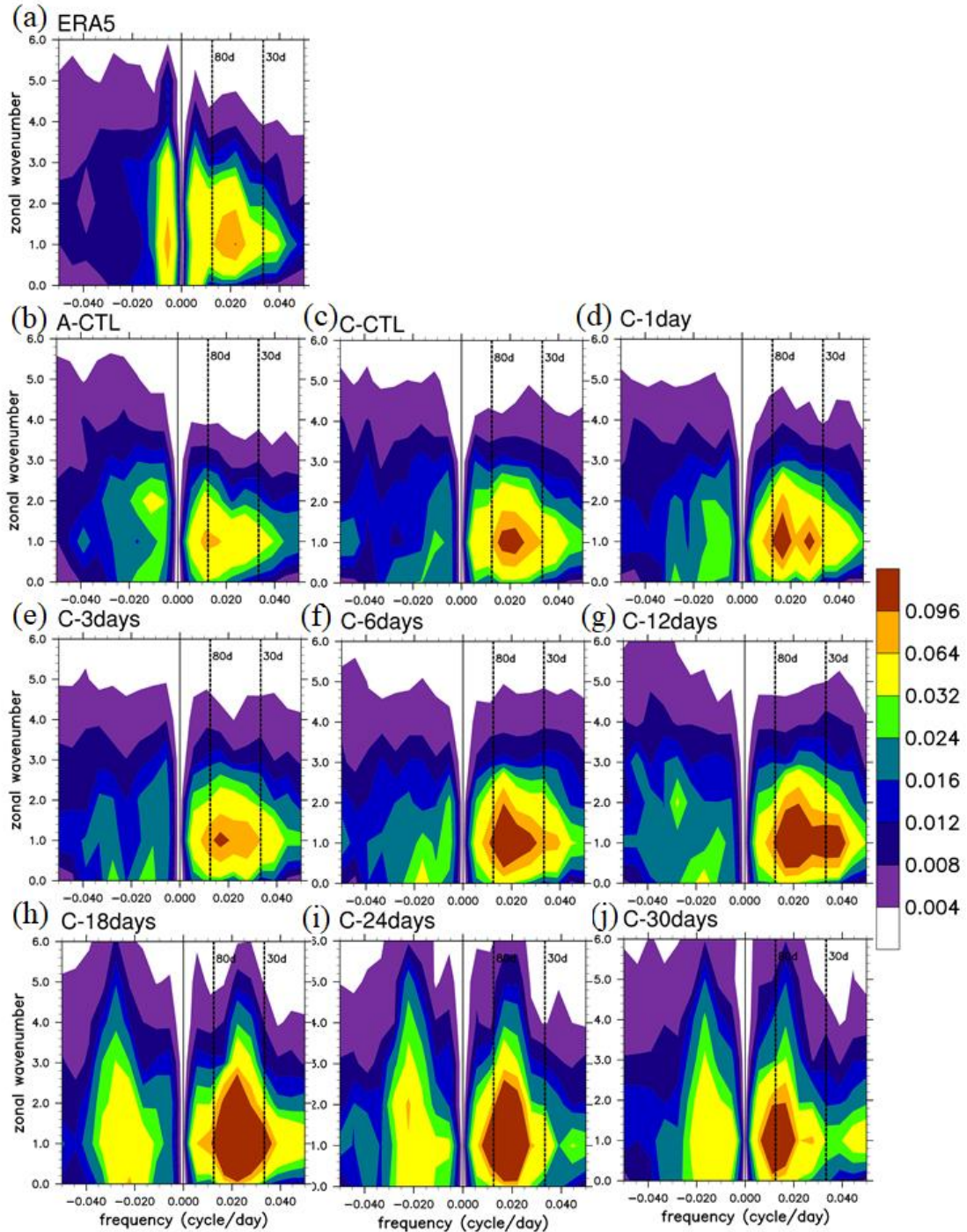
1036 **Figure 11.** The projection of each MSE component onto the ERA5 column-integrated
1037 MSE tendency at phase 5 over the MC (20° S–20° N, 90–210° E): $\langle d\text{mdt} \rangle$, $\langle \text{wdmdp} \rangle$,
1038 $\langle \text{vdm} \rangle$, Q_r , F_s , and residual; decomposition of horizontal MSE advection to zonal and
1039 meridional advection ($\langle \text{udmdt} \rangle$ and $\langle \text{vdmdy} \rangle$).

1040

1041 **Figure 12.** Filtered column-integrated vertical ($\text{J kg}^{-1} \text{s}^{-1}$, shading) and horizontal MSE
1042 advection ($\text{J kg}^{-1} \text{s}^{-1}$, contours interval 6.0), and 200-hPa wind (green vector with
1043 reference vector 3 m s^{-1}): (a) ERA5, (b) A-CTL, (c) C-CTL, (d) C-1day, (e) C-3days,
1044 (f) C-6days, (g) C-12days, (h) C-18days, (i) C-24days, and (j) C-30days. Solid-blue,
1045 dashed-red, and thick-black curves represent positive, negative, and zero values,
1046 respectively.

1047

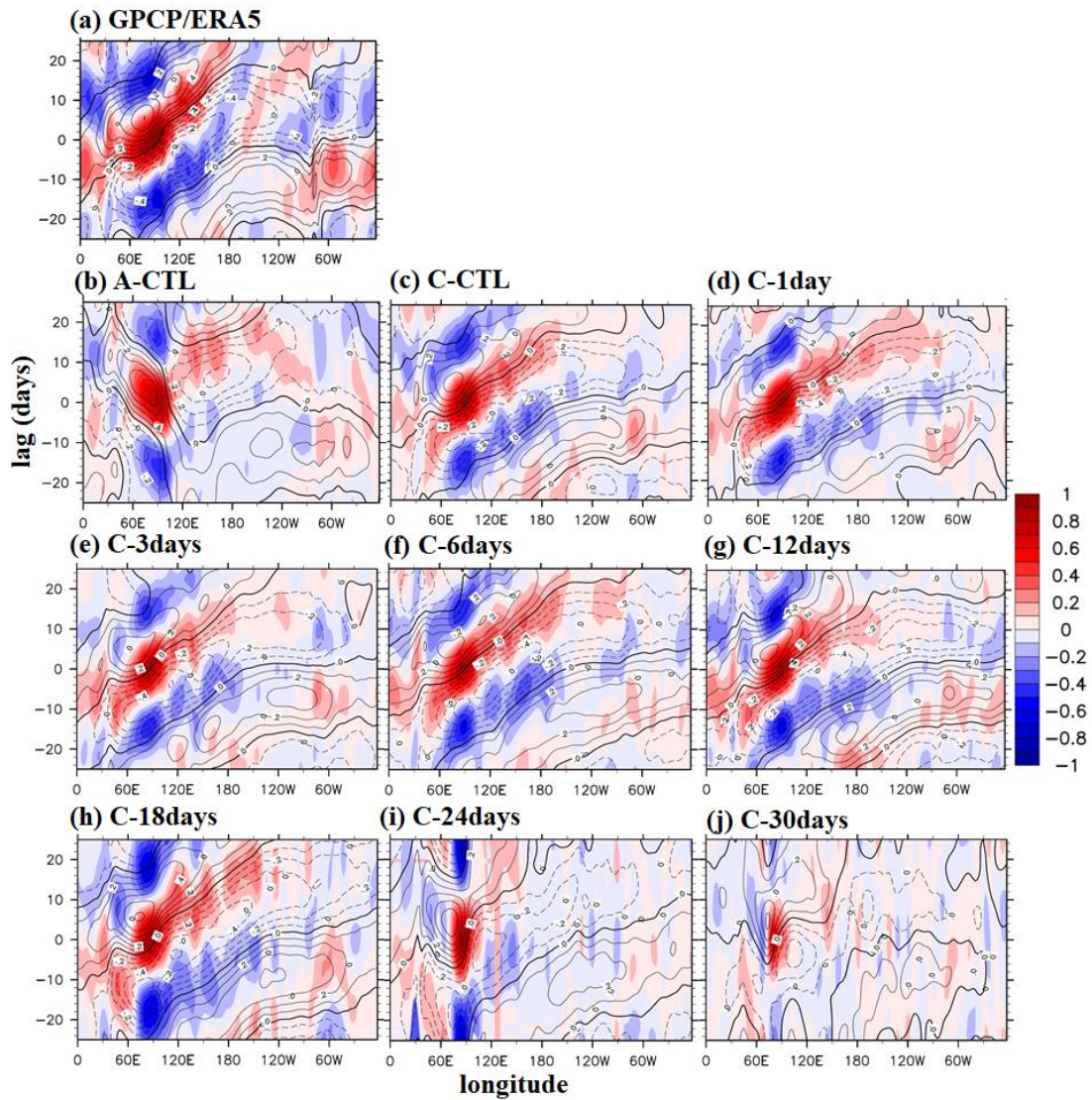
1048 **Figure 13.** Schematic diagrams illustrate the anomalous circulation and moistening
1049 processes during the eastward propagation of the MJO in experiments: (a) A-CTL, (b)
1050 high-frequency SST feedback experiments (C-CTL, C-1day, and C-3days), (c) low-
1051 frequency SST feedback experiments (C-6days, C-12days, and C-18days), and (d)
1052 C-24days and C-30days experiment. In each panel, the horizontal line represents the
1053 equator. The size of clustering gray clouds indicates the strength of convective
1054 organization. A red ellipse indicates convection-driven circulation. In the coupled
1055 simulations, light red (blue) filled ovals represent warm (cold) SST anomalies,
1056 respectively, and grass green filled rectangle represent latent heat flux. Unresolved
1057 convective processes are indicated by black dots representing low-level moisture
1058 convergence. Low-level moisture convergence into the equatorial trough is shown by
1059 light blue arrows, while midlevel moisture advection is represented by left-pointing
1060 green arrows. The deeper colors or thicker lines on the map indicate stronger anomalies
1061 of the MJO perturbations. Note: The concept of the figure is based on DeMott et al.
1062 (2014).



1063

1064 **Figure 1.** Wavenumber–frequency spectra for 850-hPa zonal wind averaged over 10°
 1065 $S-10^{\circ}$ N in boreal winter after removing the climatological mean seasonal cycle.
 1066 Vertical dashed lines represent periods at 80 and 30 days. (a)–(j) are from ERA5
 1067 reanalysis, A-CTL, C-CTL, C-1day, C-3days, C-6days, C-12days, C-18days, C-
 1068 24days, and C-30days, respectively.

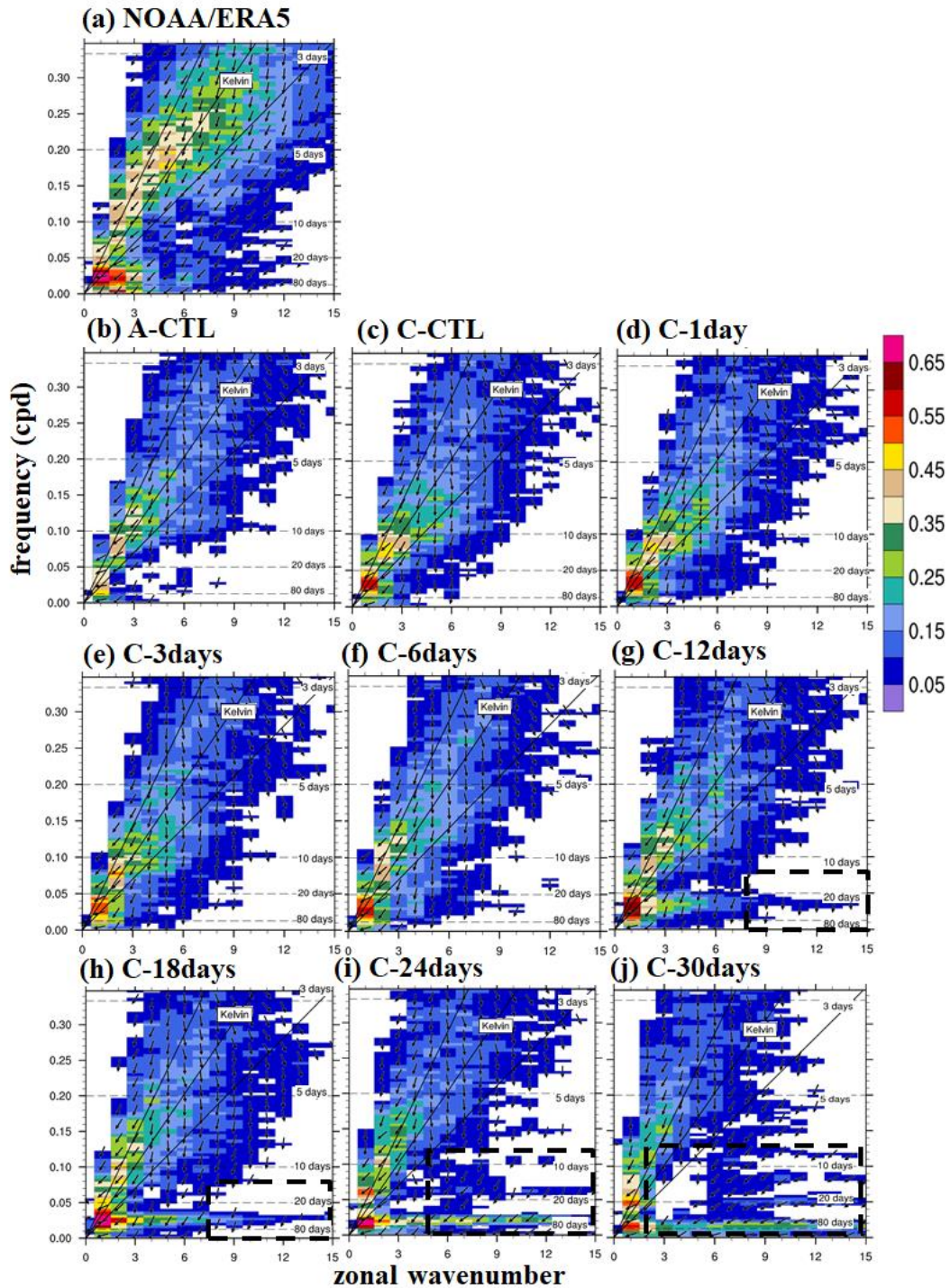
1069



1070

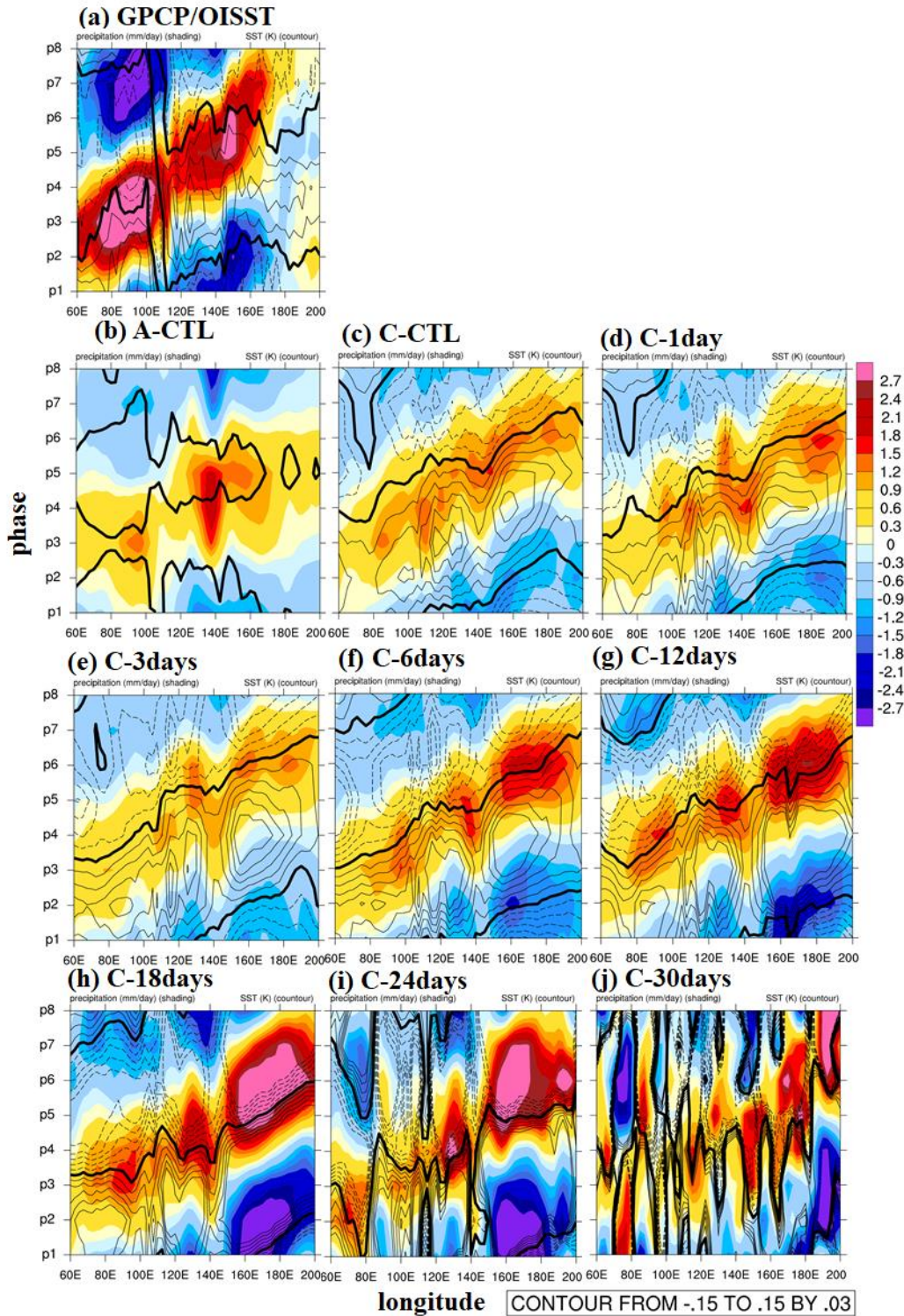
1071 **Figure 2.** Hovmöller diagrams of correlation between precipitation averaged over 10°
 1072 S–5° N, 75–100° E and precipitation (color) and 850-hPa zonal wind (contour)
 1073 averaged over 10° N–10° S. (a)–(j) are arranged in the same order as in Fig. 1 for
 1074 GPCP/ERA5 and all experiments. All data are 20–100-day bandpass filtered.

1075



1076

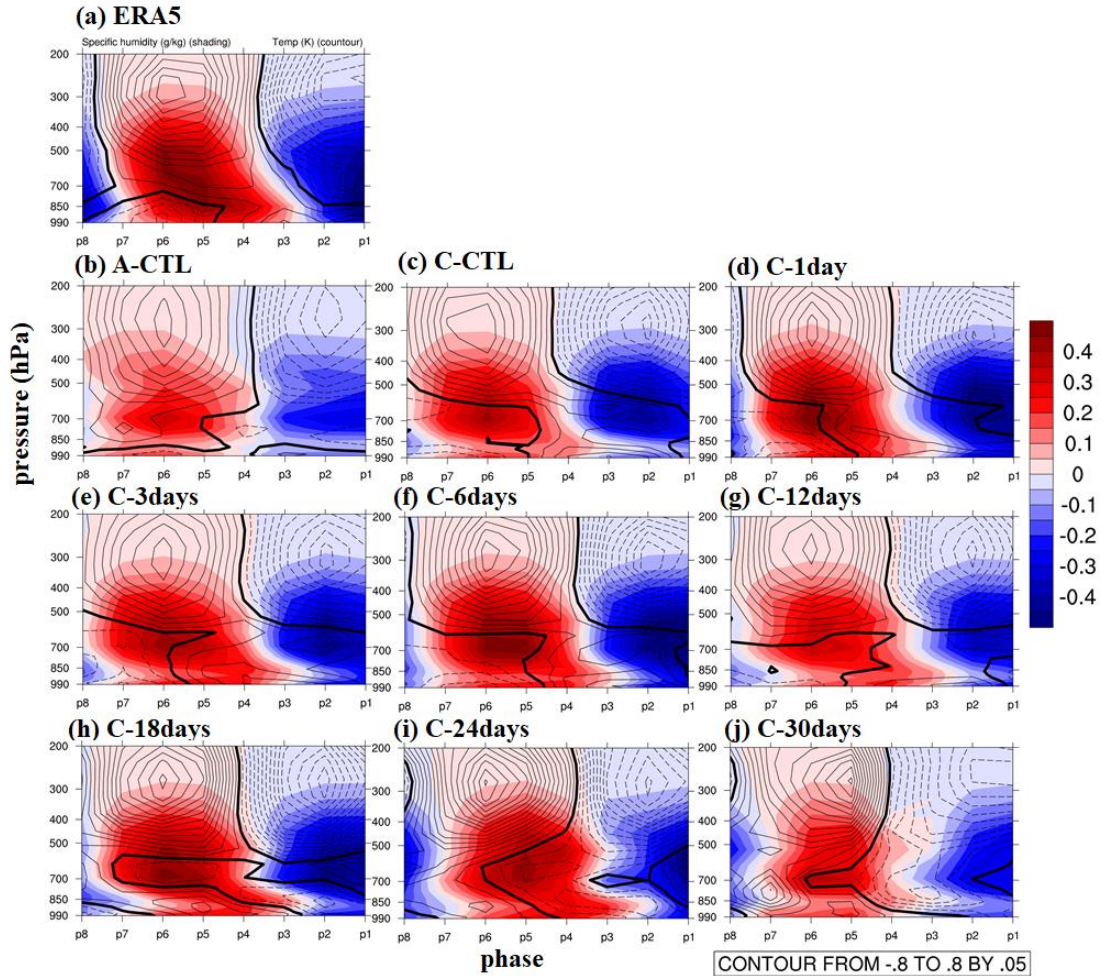
1077 **Figure 3.** Zonal wavenumber–frequency power spectra of anomalous OLR (colors) and
 1078 phase lag with U850 (vectors) for the symmetric component of tropical waves, with the
 1079 vertically upward vector representing a phase lag of 0° with phase lag increasing
 1080 clockwise. Three dispersion straight lines with increasing slopes represent the
 1081 equatorial Kelvin waves (derived from the shallow water equations) corresponding to
 1082 three equivalent depths, 12, 25, and 50 m, respectively. (a)–(j) arrange in order are same
 1083 order as in Fig. 1 for NOAA/ERA5 and all experiments.



1084

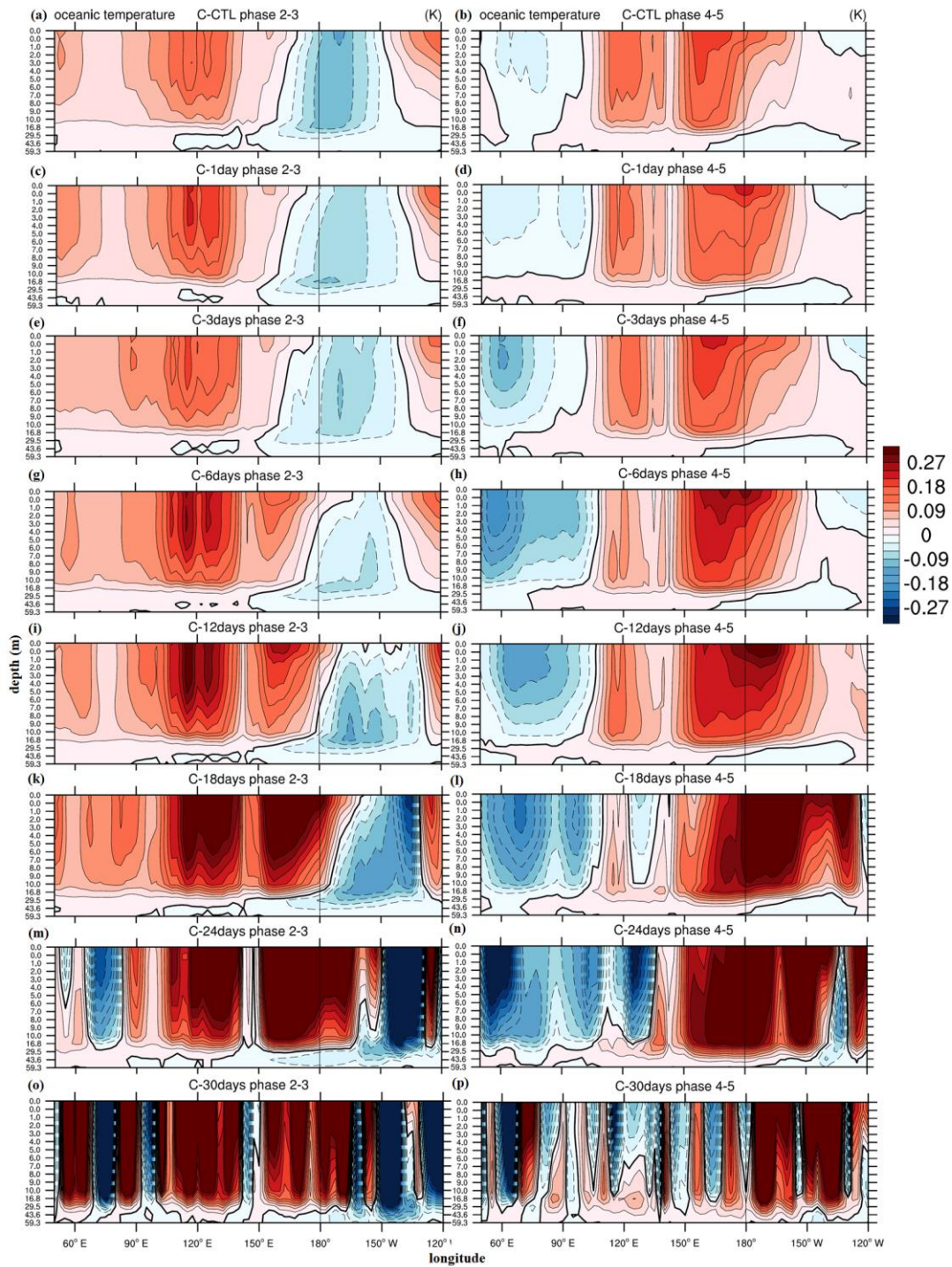
1085 **Figure 4.** Phase-longitude Hovmöller diagrams of 20–100-day filtered precipitation
 1086 (mm day⁻¹, shaded) and SST anomaly (K, contour) averaged over 10° N–10° S from
 1087 phase 1 to 8. Contour interval is 0.03; solid, dashed, and thick-black lines represent
 1088 positive, negative, and zero values, respectively. (a)–(j) are arranged in the same order
 1089 as in Fig. 1 for NOAA/ERA5 and all experiments.

1090



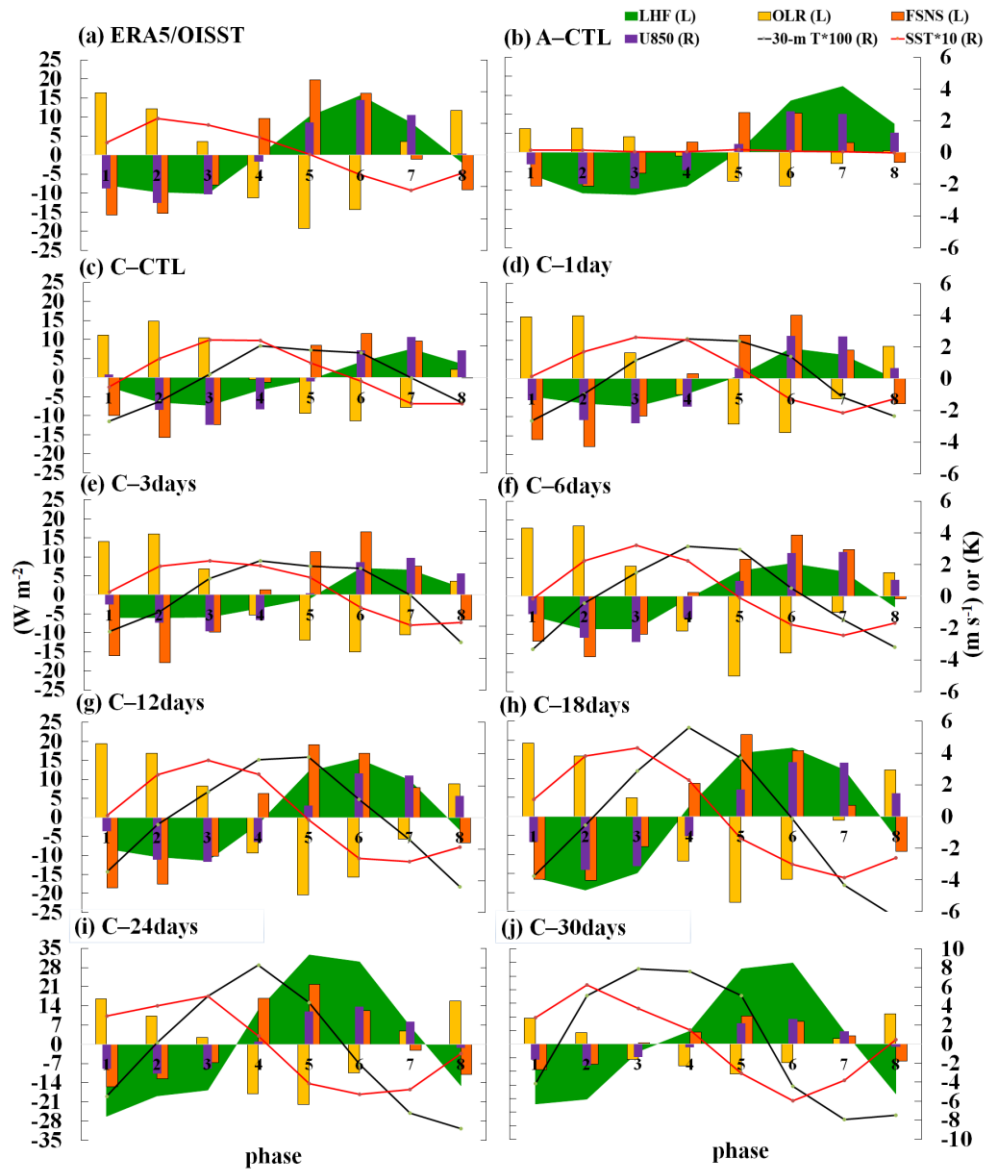
1091
 1092
 1093
 1094
 1095
 1096
 1097

Figure 5. Phase-vertical Hovmöller diagrams of 20–100-day specific humidity (shading, g kg^{-1}) and air temperature (contoured, K) averaged over $5\text{--}20^\circ\text{ S}$, $120\text{--}150^\circ\text{ E}$; solid, dashed, and thick-black curves are positive, negative, and zero values, respectively. (a)–(j) are arranged in the same order as in Fig. 1 for NOAA/ERA5 and all experiments.



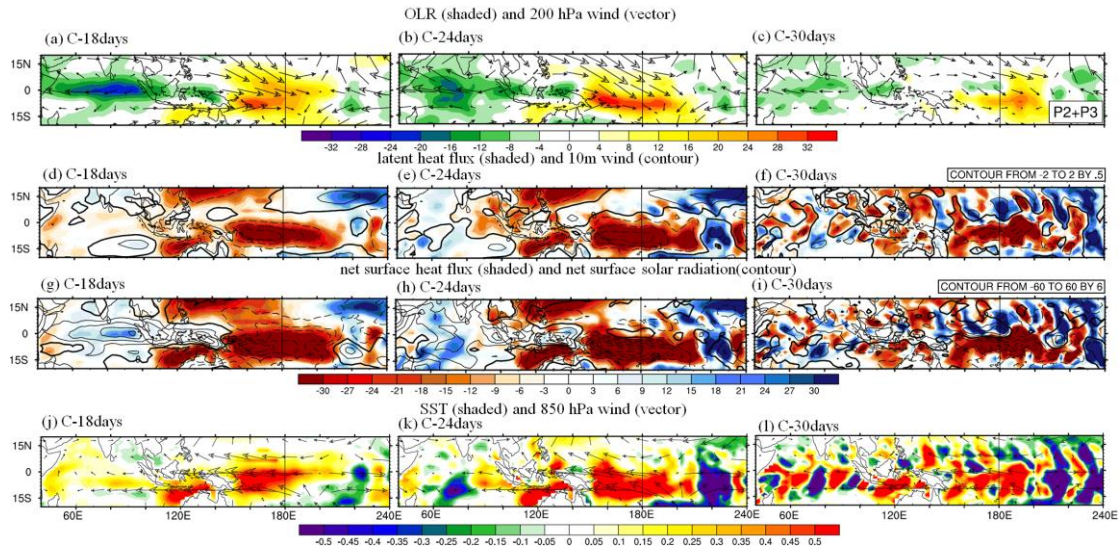
1099

1100 **Figure 6.** The 20–100-day filtered oceanic temperature (K, shaded and contour, interval
 1101 0.03) at phase 2–3 (Left column) and phase 4–5 (Right column) averaged over 0–15°
 1102 S between 0 and 60 m depth. (a)–(b) are from C–CTL, (c)–(d) are from C–1day, (e)–(f)
 1103 are from C–3days, (g)–(h) are from C–6days, (i)–(j) are from C–12days, (k)–(l) are
 1104 from C–18days, (m)–(n) are from C–24days, and (o)–(p) are from C–30days.



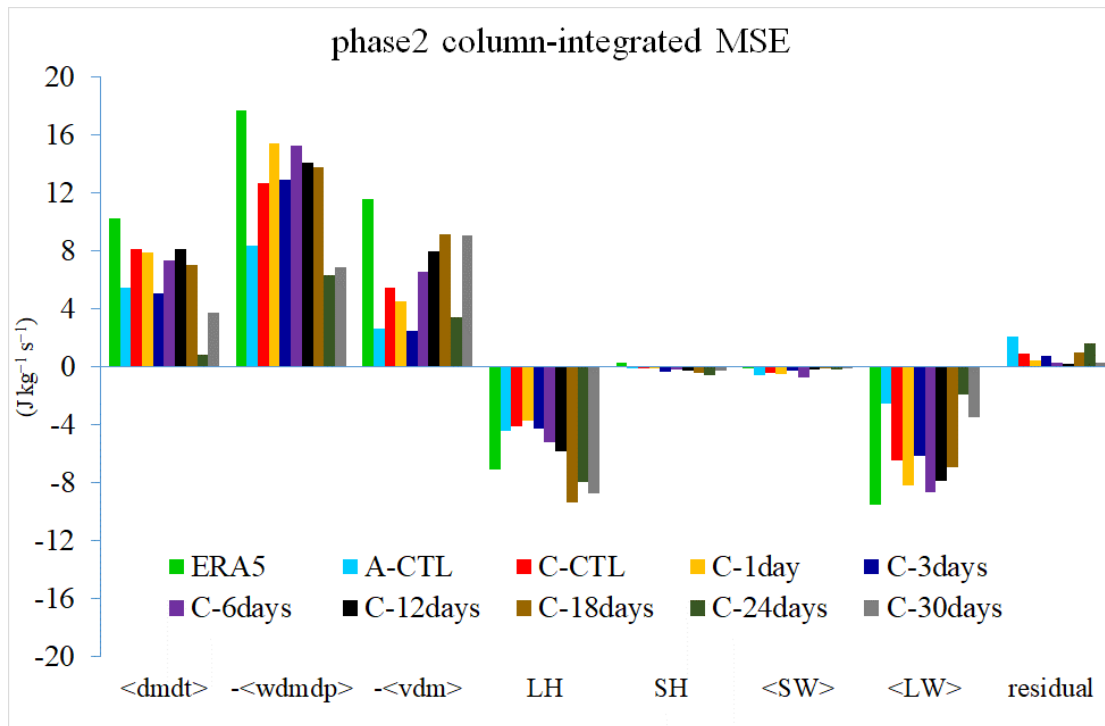
1105

1106 **Figure 7.** The lead-lag relationship between MJO-related atmosphere and SST
 1107 variation from phase 1 to 8 averaged within 110–130° E and 5–15° S. The variables
 1108 analyzed include 20-100-day filtered LHF, green shading), OLR (yellow bar chart),
 1109 FSNS, (orange bar chart), U850 (purple bar chart), 30-m T (multiplied by 100, black
 1110 line), and SST (multiplied by 10, orange line). Variables denoted with L (R)
 1111 by the left (right) y-axis. (a)–(j) are from ERA5/OISST reanalysis, A-CTL, C-CTL, C-
 1112 1day, C-3days, C-6days, C-12days, C-18days, C-24days, and C-30days, respectively.



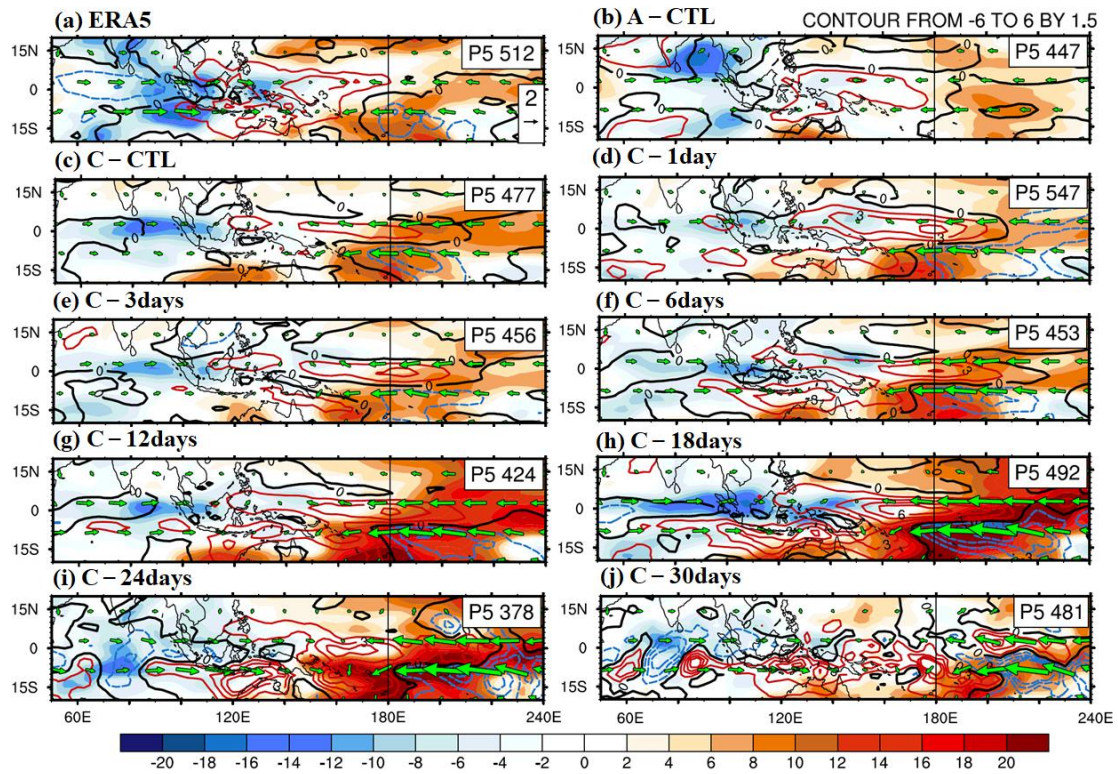
1113

1114 **Figure 8.** Averaged 20–100-day filtered fields at phase 2–3. (Upper row) OLR (W m^{-2} ,
 1115 shaded) and 200 hPa zonal and meridional wind anomaly (m s^{-1} , vector with reference
 1116 vector shown at the top right corner, latent heat flux (W m^{-2} , shaded, positive
 1117 representing upward), and 10-m wind anomaly (m s^{-1} , contour interval 0.5). (Second
 1118 row) net surface heat flux (W m^{-2} , shaded) and net solar radiation (W m^{-2} , contour
 1119 interval 6). (Third row) SST (K, shaded) and 850 hPa zonal and meridional wind
 1120 anomaly (m s^{-1} , vector with reference vector shown at the top right corner. The number
 1121 of days used to generate the composite is shown at the bottom right corner. (a), (d), (g)
 1122 and (j) are from C–18days; (b), (e), (h) and (k) are from C–24days, and (c), (f), (i) and
 1123 (l) are from C–30days, respectively. Solid, dashed, and thick-black lines represent
 1124 positive, negative, and zero values, respectively.



1126

1127 **Figure 9.** Averaged 20–100-day filtered column-integrated MSE budget terms
 1128 ($\text{J kg}^{-1} \text{s}^{-1}$) in $10^\circ \text{ S}–0^\circ \text{ N/S}$, $120–150^\circ \text{ E}$ for ERA5 and all model simulations.
 1129 Colors represent different datasets: green for REA5, light blue for A–CTL, red, orange
 1130 and navy blue for high-frequency experiments (C–CTL, C–1day, and C–3days,
 1131 respectively), purple, black, dark brown, dark green, and dark gray for low-frequency
 1132 experiments (C–6days, C–12days, C–18days, C–24days, and C–30days, respectively).
 1133 The bars from left to right represent MSE tendency ($\langle \text{dmdt} \rangle$), vertical MSE advection
 1134 ($-\langle \text{wdmdp} \rangle$), horizontal MSE advection ($-\langle \text{vdm} \rangle$), surface latent heat flux (LH),
 1135 surface sensible heat flux (SH), shortwave radiation flux ($\langle \text{SW} \rangle$), longwave radiation
 1136 flux ($\langle \text{LW} \rangle$), and residual terms.

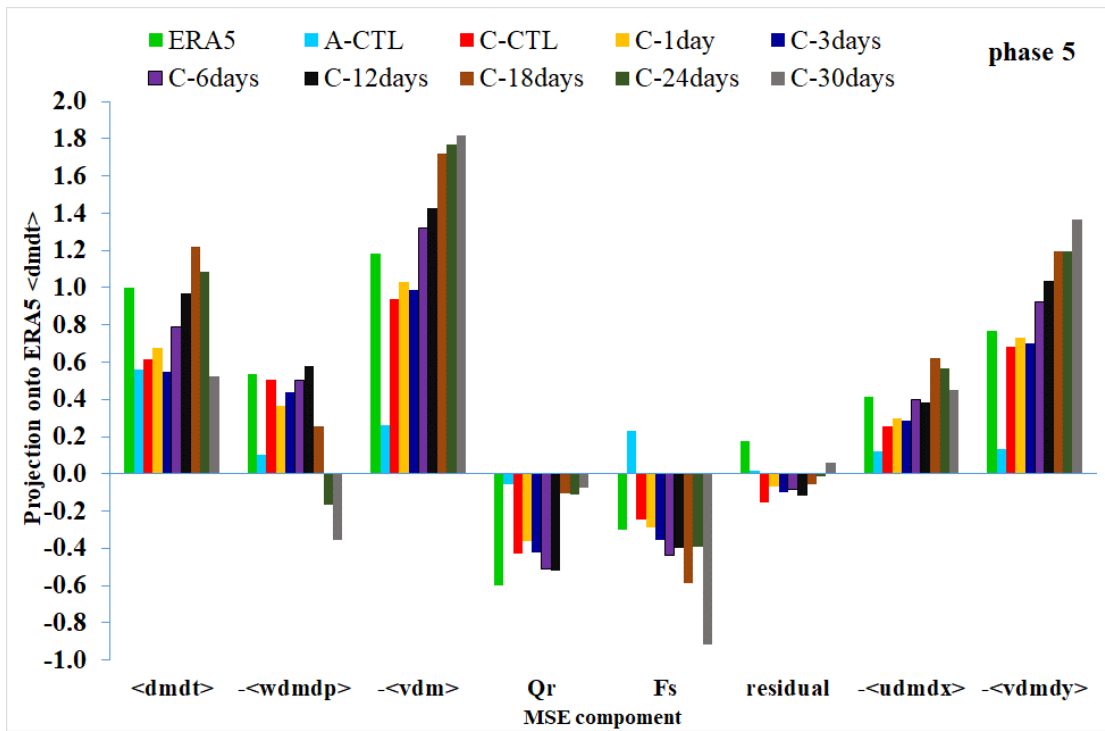


1138

1139 **Figure 10.** Filtered the column-integrated MSE tendency ($\text{J kg}^{-1} \text{s}^{-1}$, shading),
 1140 precipitation (mm d^{-1} , contours interval 1.5) and 850-hPa wind (green vector, reference
 1141 vector 2 m s^{-1}) in phase 5: (a) ERA5, (b) A-CTL, (c) C-CTL, (d) C-1day, (e) C-3days,
 1142 (f) C-6days, (g) C-12days, (h) C-18days, (i) C-24days, and (j) C-30days. Solid-red,
 1143 dashed-blue, and thick-black curves represent positive, negative, and zero values,
 1144 respectively.

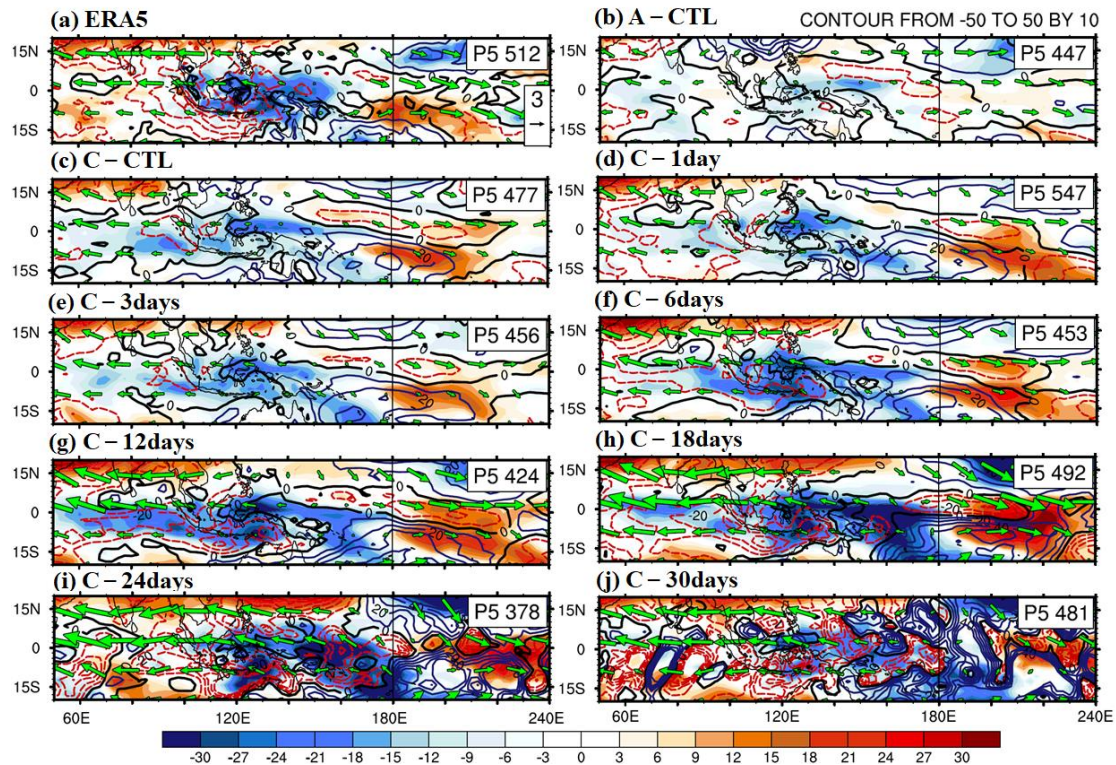
1145

1146



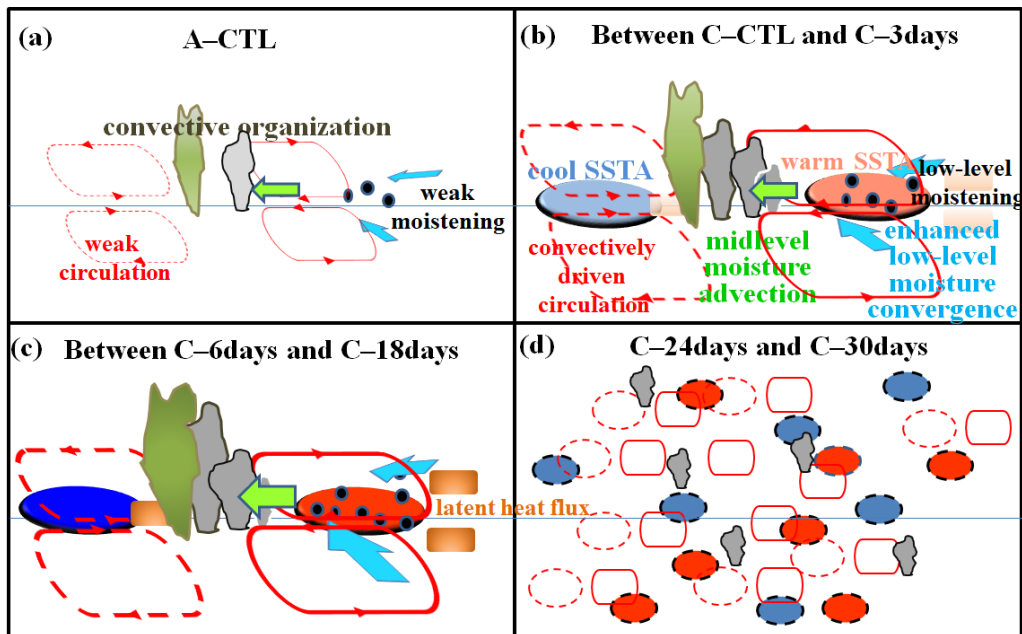
1147

1148 **Figure 11.** The projection of each MSE component onto the ERA5 column-integrated
1149 MSE tendency at phase 5 over the MC (20° S– 20° N, 90 – 210° E): <dmdt>, -
1150 <wdmdp>, -<vdm>, Qr, Fs, and residual; decomposition of horizontal MSE advection
1151 to zonal and meridional advection (-<udmdx> and -<vmdy>).



1152

1153 **Figure 12.** Filtered column-integrated vertical ($\text{J kg}^{-1} \text{s}^{-1}$, shading) and horizontal MSE
 1154 advection ($\text{J kg}^{-1} \text{s}^{-1}$, contours interval 6.0), and 200-hPa wind (green vector with
 1155 reference vector 3 m s^{-1}): (a) ERA5, (b) A-CTL, (c) C-CTL, (d) C-1day, (e) C-3days,
 1156 (f) C-6days, (g) C-12days, (h) C-18days, (i) C-24days, and (j) C-30days. Solid-blue,
 1157 dashed-red, and thick-black curves represent positive, negative, and zero values,
 1158 respectively.



1160

1161 **Figure 13.** Schematic diagrams illustrate the anomalous circulation and moistening
 1162 processes during the eastward propagation of the MJO in experiments: (a) A-CTL, (b)
 1163 high-frequency SST feedback experiments (C-CTL, C-1day, and C-3days), (c)
 1164 low-frequency SST feedback experiments (C-6days, C-12days, and C-18days), and (d)
 1165 C-24days and C-30days experiment. In each panel, the horizontal line represents the
 1166 equator. The size of clustering gray clouds indicates the strength of convective
 1167 organization. A red ellipse indicates convection-driven circulation. In the coupled
 1168 simulations, light red (blue) filled ovals represent warm (cold) SST anomalies,
 1169 respectively, and grass green filled rectangle represent latent heat flux. Unresolved
 1170 convective processes are indicated by black dots representing low-level moisture
 1171 convergence. Low-level moisture convergence into the equatorial trough is shown by
 1172 light blue arrows, while midlevel moisture advection is represented by left-pointing
 1173 green arrows. The deeper colors or thicker lines on the map indicate stronger anomalies
 1174 of the MJO perturbations. Note: The concept of the figure is based on DeMott et al.
 1175 (2014).